MULTI-WAVELENGTH ALL-OPTICAL 2R REGENERATION

by

PALLAVI GOVIND PATKI

Presented to the Faculty of the Graduate School of

The University of Texas at Arlington in Partial Fulfillment

of the Requirements

for the Degree of

DOCTOR OF PHILOSOPHY

THE UNIVERSITY OF TEXAS AT ARLINGTON

August 2010

Dedicated to my dear parents and

my little sisters Jani and Revati

ACKNOWLEDGEMENTS

First and foremost, I would like to thank my advisor, Dr. Michael Vasilyev for inspiring and supporting me during my PhD research work. I am grateful to him for giving me the opportunity to work on state-of- the-art testbed in our lab. I am fortunate to have worked with him as he is a kind advisor and great teacher.

I express my sincere gratitude to Dr Nikolai Stelkmakh, who has also guided me during my research work. He has always been very approachable and willing to clear my doubts and questions. I will always remember him for his words of encouragement and constructive feedback while preparing for conference presentations. I also thank Dr. T. I. Lakoba from University of Vermont, who has been part of this research work. His modeling results were vital for validation of our experimental results.

I would like to thank members on my committee, Profs. R. Magnusson, J.C Chiao and W. Zhou for their time and interest in my research.

There are many people whose company I have enjoyed at UTA. I thank my lab members Sarath, Muthu , Lei and Veronica for their help in completing this research work . Special thanks to Muthu and Sarath for their friendship and healthy never ending discussions we had in the lab.

I would also like to express my gratitude to Gail Paniuski and Anne Lewiston for their support and prompt response to all my administrative queries.

I am grateful to my supervisor at Corning Inc, Richard Vodhanel for his interest and feedback in my research. I truly enjoyed the company of John Downie and Jason Hurley at Corning Inc. Their understanding was essential in me finishing this thesis. I am also thankful to Professor John Cartledge from Queen's University, for his feedback on my research.

I gratefully acknowledge the support provided to this research by the National Science Foundation and Texas Higher Education Coordinating Board Advanced Research Program. I am thankful to Valeria L. DaSilva and Scott Bickham of Corning Inc. for providing the dispersion compensating fiber, one of the most essential components of my 2R regenerator. I also acknowledge Preston Young at Photodigm for providing test equipment for my multi-channel experiments.

This PhD would have come true without the unrelenting support of my parents and husband. They have made a lot of sacrifices for this dream to come true. My gratitude goes to my sweet sisters for their love and encouragement. They have been my emotional punching bag all these years. Last but not least, I must thank my cousins, uncle, aunt and in-law family members for their support while I pursued my research.

July 5, 2010

ABSTRACT

MULTI-WAVELENGTH ALL-OPTICAL 2R REGENERATION

Pallavi Govind Patki, PhD

The University of Texas at Arlington, 2010

Supervising Professor: Michael Vasilyev

We experimentally demonstrate, for the first time to our knowledge, simultaneous all-optical 2R regeneration of multiple WDM channels.

In the recent work [1], our group has proposed an all-optical 2R regeneration scheme capable of handling multiple WDM channels simultaneously. Our proposed multi-channel regenerator is a modified configuration of Mamyshev's 2R regenerator [2], in which a conventional highly-nonlinear-fiber (HNLF) is replaced by a novel dispersion-managed nonlinear medium. The proposed multi-channel regeneration scheme uses multiple concatenated dispersion-managed sections, where each dispersion-managed section contains a piece of HNLF and a periodic-group-delay device (PGDD). For the proof-of-principle demonstration of the regenerator we have built a recirculating loop, where, instead of cascading multiple identical HNLF-PGDD sections, we use only one such section and pass the signal through it multiple times.

In this dissertation, we present our experimental results on single- and multi-channel all-optical 2R regeneration. We experimentally demonstrate single-channel 2R regeneration in a dispersion-managed configuration of Mamyshev's regenerator. The experimentally observed 3dB eye-opening improvement confirms that single-channel performance is not degraded by dispersion management. The multi-channel regeneration experiments were performed with as many as 12 channels (12 x 10 Gb/s), and as few as 2 channels (2 x 10 Gb/s). We discuss our experimental results on 2-, 8-, and 12-channel all-optical regeneration. All 12 channels demonstrate eye-opening improvement better than 2 dB. We have experimentally characterized the performance of our regenerator with respect to the number of neighboring channels. Our experimental results show that 'unlike the prior attempts of multi-channel all-optical regeneration by other groups' our dispersion management technique overcomes the regenerator degradations by inter-channel four-wave mixing (FWM) and cross-phase modulation (CPM).

TABLE OF CONTENTS

LIST OF ILLUSTRATIONS

Figure Page

LIST OF TABLES

CHAPTER 1

INTRODUCTION

As signal propagates inside an optical fiber, the quality of the signal is degraded due to linear and nonlinear impairments, and accumulation of noise, thereby requiring regeneration periodically along the link. A regenerator placed along the transmission link restores the signal quality to its original form. Signal regeneration is achieved either by employing conventional electronic repeaters or by using all-optical regenerators periodically along the transmission link. A conventional electronic regenerator consists of an optical transmitter-receiver pair and is based on opto-electro-opto (OEO) conversion. An optical signal is first converted to an electrical signal, electronically regenerated, converted back again to its optical form, and retransmitted. In high capacity optical systems employing multiple WDM channels, electronic regeneration requires separate repeaters for each channel and is therefore, very bulky and expensive. At symbol rates of 80 Gb/s and beyond, all-optical regeneration is the only means to regenerate data, as electronic processing is not applicable at such high bit rates. All-optical regeneration technique does not suffer any time response limitation, as the signal processing is performed in optical domain. Optical regeneration is classified as: 1R (reamplifying), 2R (reamplifying + reshaping), and 3R (reamplifying + reshaping + retiming). In [2], a simple and robust all-optical 2R regeneration technique based on self-phase modulation (SPM) and band-pass filtering was proposed. Here, the signal

propagates through a piece of highly nonlinear fiber (HNLF) which causes the signal spectrum to broaden due to self-phase modulation (SPM). Then, the broadened spectrum is filtered out by an optical band pass filter (OBPF) whose frequency is shifted with respect to the input signal. This method suppresses the noise in "zeros" and the amplitude fluctuations in "ones" of return-to-zero (RZ) optical data streams. In order to compete with conventional electronic repeaters, all-optical regenerators must be scalable with the number of WDM channels. However, simultaneous multi-channel regeneration remains a challenge as the operation of an all-optical regenerator fundamentally relies on strong nonlinear optical effects which cause the cross-talk among the WDM channels.

The solution to multi-channel all-optical 2R regeneration has been proposed in [1]. Our proposed 2R regenerator scheme employs a dispersion map that enables simultaneous regeneration of multiple WDM channels by suppressing inter-channel four-wave mixing (FWM) and cross-phase modulation (CPM) while achieving strong self-phase modulation (SPM). The approach [1] uses multiple HNLF sections with high normal dispersion, separated by dispersion compensating periodic-group-delay devices (PGDDs). PGDDs are the key components of our proposed generation scheme, and the demonstration of this regenerator requires at least 16 PGDDs. For the proof-of-principle demonstration, we put a single PGDD and a piece of HNLF into a recirculating loop through which light will pass multiple times.

This dissertation focuses on experimental demonstration of simultaneous 2R regeneration of multiple WDM channels. For practical demonstration of multi-channel

2R regeneration, we need to experimentally prove two key points. First step is to experimentally show that for single channel, our dispersion-management scheme does not affect the regeneration. In single-channel regeneration experiment, we do not need the periodicity of PGDD response and thus, instead of PGDD we will use a combination of standard single-mode fiber (SSMF) and non-zero dispersion-shifted fiber (NZDSF) to compensate the dispersion of HNLF. The second step is to experimentally illustrate that for simultaneous multiple channel regeneration, inter-channel nonlinearities are strongly suppressed by our PGDD-based dispersion-management scheme. This effort has required designing a recirculating loop to work with only few hundred meters of fiber.

The structure of this dissertation is as follows. The second chapter gives it gives an introduction to all-optical regeneration, and focuses on SPM-based regenerators. In addition, it gives an overview of linear and nonlinear processes in optical fiber and impact of these effects on WDM optical systems. The third chapter describes the working principle of Mamyshev's 2R regenerator and explains the concept of our proposed multi-channel 2R regenerator scheme. It also discusses dispersion compensation using PGDD. In the fourth chapter, we discuss the design and experimental realization of our recirculating-loop testbed and trigger settings for the successful operation of the loop. Finally, we discuss the experimental setup and results of single-, 2- 8- and 12-channel all-optical 2R regeneration. The fifth chapter discusses the future scope of this research work. The last chapter summarizes the dissertation. Appendix A describes operation of Teraxion ClearSpectrum^{TM}-TDC using Wavelength

Electronics temperature controllers and, appendix B summarizes the important settings on devices employed in our 2R regeneration experimental testbed.

CHAPTER 2

OVERVIEW OF ALL-OPTICAL REGENERATION

2.1 WDM Optical Transmission Systems

Today optical fibers are the medium of choice for transmission of data at the highest capacity over the longest possible distance. The widespread use of optical fibers for long-haul systems is driven by the unique properties of fibers in the 1550 nm wavelength band: very low attenuation (0.2 dB/km), large potential bandwidth (>1 THz), and low price. The usable bandwidth of a single-mode optical fiber that can be utilized for telecommunication is in the wavelength range of 1280 nm to 1650 nm. Thus the intrinsic transmission capacity of the single-mode fiber is about 50 THz. In practice, the spectral efficiency of optical communication systems using on-off keying modulation technique is about 0.4 bits/s/Hz [3]. Using this value of spectral efficiency the maximum capacity of optical fiber is about 20 Tb/s. However, only a small percent of the total bandwidth of a single-mode fiber has been exploited (10 Gb/s signal uses only 0.05% of this total bandwidth). There are fundamentally two techniques of increasing the transmission capacity: time-division-multiplexing and wavelength-division-multiplexing. In time division multiplexing (TDM) the required transmission bit rate is achieved by multiplexing many low-speed data streams into a higher-speed stream in time domain. TDM requires higher-speed electronics. Today, the highest transmission rate in commercially available systems using TDM technology is 40 Gb/s.

Another way to increase the transmission capacity is by wavelength division multiplexing (WDM). WDM technique takes *N* signals at different wavelengths, each of *B* Gb/s, and multiplexes them into a single fiber with a total aggregate rate of *NB* Gb/s. Thus WDM makes a simple fiber look like multiple "virtual" fibers, with each virtual fiber carrying a single data stream [3]. The overall capacity of the WDM systems is equal to the total number of channels multiplied by the channel bit rate. As the signal propagates through an optical fiber, there is decay in the signal strength and hence the signal must be amplified after regular intervals. The amplification can be done with an electronic repeater. For multi-channel WDM systems designed for long-haul transmissions, each single channel would require a separate repeater. Thus, for an *N* - channel system, *N* repeaters are required and, as a result, until mid 1990s, WDM systems were not economically feasible. With the advent of erbium-doped fiber amplifiers (EDFAs), it became possible to amplify multiple WDM signals simultaneously by one EDFA, and thus EDFAs started replacing electronic repeaters in the optical transmission systems. Because of their large gain, low noise, and high output powers, typical EDFAs can handle about 100 WDM channels with amplifier spacing of 100 km, thereby significantly reducing the cost of transmission systems [4]. This benefit of EDFA comes at the expense of many limitations when deployed in WDM systems. First of all, the usable bandwidth for WDM systems strongly depends on the availability of optical amplifiers in that wavelength range. Also, in lightwave systems several amplifiers are cascaded and each amplifier amplifies not only the optical signal but also the amplified spontaneous noise (ASE) noise. Thus, as the signal travels down the

cascade of amplifiers, it becomes necessary to deal with the optical signal to noise ratio (OSNR) degradation due to accumulation of amplifier noise over the entire link. Furthermore, the large multi-channel signal power in the fiber brings about nonlinearities in the fiber, causing crosstalk among the different WDM channels and increasing signal distortions. The dispersion and nonlinear effects are interrelated with each other and thus dispersion management becomes essential. WDM systems today mostly operate in the C-band or 1550 nm window (1530 nm to 1565 nm) due to the minimum attenuation of single-mode silica fibers in that region and due to the main gain band of EDFA. In addition to the C-band, the L-band (1565 nm to 1605 nm) has emerged as a new wavelength window for WDM systems with the expansion of gain band of EDFA. Another parameter of interest in the WDM systems is the channel spacing, which is the spacing between two neighboring channels or wavelengths. In WDM systems, to avoid crosstalk effects arising due to interference between neighboring channels, as well as the distortion of channel itself, the signal bandwidth needs to be sufficiently smaller than the channel spacing.

This chapter mainly describes limitations in transmission of light in optical fibers due to linear and nonlinear effects. It starts with a brief explanation of fiber attenuation. It is followed by discussion of dispersion in single-mode fibers. The nonlinear effects in optical fibers are discussed in section 2.4. It explains the origin of fiber nonlinearity and describes three nonlinear processes: self-phase modulation (SPM), cross-phase modulation (CPM), and four-wave mixing (FWM). The last section

of this chapter is devoted to all-optical regeneration and focuses on SPM-based regenerators.

2.2 Attenuation

Attenuation is the loss of light power as the signal propagates through an optical fiber and the amount of power loss during the transmission is given by [5],

$$P_{out} = P_{in} e^{-\alpha L} \tag{2.1}$$

Here P_{in} is the input power, P_{out} is the output power at the end of the fiber of length L, and the parameter α is attenuation constant. Attenuation in optical fiber is caused primarily due to material absorption and Rayleigh scattering. Material absorption is caused by the intrinsic properties of silica and the impurities in the fiber. Rayleigh scattering arises because of small variations in the density of glass, as it cools during manufacturing. The resulting variations are microscopic, smaller than the wavelengths used, and therefore scatter light in all directions. The Rayleigh scattering loss varies as λ^{-4} and thus predominantly affects short wavelengths. While Rayleigh scattering limits the use of wavelengths below 800 nm, the material absorption increases significantly above 1700 nm. For silica based optical fibers, three low-loss windows within the infrared spectrum have been exploited: 850 nm, 1310 nm and 1550 nm. The wavelength band near 850 nm (α = 1.5 dB/km) was used mostly for short-range, multi-mode applications. The large attenuation spike, due to absorption by water molecules, defines two low-loss windows: the O-band (original band) and the C-band (conventional band). In the O-band, centered around 1310 nm, the single-mode fibers have $\alpha \sim 0.3$ dB/km, and in the C-band the attenuation is minimal with $\alpha \sim 0.19$ dB/km [5].

2.3 Dispersion in single-mode fibers

A linear isotropic medium is characterized by a linear relationship between the polarization density P and the electric field E,

$$P = \varepsilon_0 \chi E \tag{2.2}$$

Here, ε_0 is the dielectric permittivity of free space and χ is the linear susceptibility of the medium. P is the induced electric polarization of the material, also called dielectric polarization. The dielectric polarization can be viewed as the output of a linear system to the applied electric field as input. However, the response $\varepsilon_0\chi$ of silica medium to the applied electric field is not instantaneous i.e., the value of P at time t depends not only on the value of E at time t but also on the values of E before time t. Therefore, χ in Eq. (2.2) is frequency dependent $\chi(\omega)$ and this is the origin of chromatic dispersion [3]. The refractive index is related to the susceptibility as [3],

$$n^2(\omega) = 1 + \chi(\omega) \tag{2.3}$$

Since the susceptibility is frequency dependent, so is the refractive index. For single-mode fiber (SMF), the main source of dispersion is the Group-Velocity Dispersion (GVD). The Group-Velocity Dispersion (GVD) in SMF comes from the fact that the refractive index of the optical fiber is frequency dependent, or is a function of the wavelength, $n(\lambda)$. Therefore, a specific spectral component, with wavelength λ, traveling through a SMF of length L, would arrive at the output end of the fiber after a time delay of $T = L / v_g(\lambda)$, where $v_g(\lambda)$ is the group velocity. Since different spectral components associated with the pulse propagate with different speeds given by $v_g(\lambda) =$

c / n_g (λ), where n_g (λ) $= n\left(1-\lambda\frac{dn}{d\lambda}\right)$, they do not arrive at the same time at the fiber output and hence lead to pulse broadening. This is commonly referred to as chromatic dispersion. The parameter, β_2, determines how much an optical pulse would broaden up on propagation inside the fiber. Quite often, an alternative parameter D is used to characterize the dispersion instead of β_2. D is related to β_2 by,

$$D = \frac{d}{d\lambda}\left(\frac{1}{v_g(\lambda)}\right) = -\frac{2\pi c}{\lambda^2}\beta_2 \tag{2.4}$$

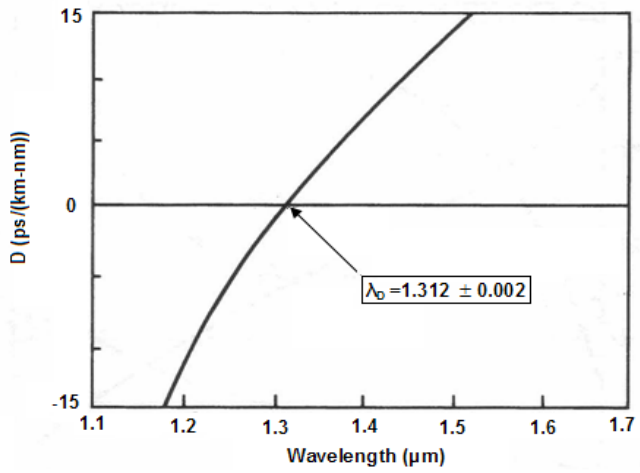

Fig. 2.1. Measured dependence of dispersion parameter D on wavelength for a standard single-mode fiber. (Revised from Fig. 1.6 in Ref. [5]).

Figure 2.1 shows the measured dependence of total dispersion parameter D on wavelength for the SSMF [5]. The wavelength λ_0 (Fig. 2.1), is known as zero-dispersion wavelength, the wavelength at which β_2 and D become zero. For $\beta_2>0$ (or $D<0$), i.e. for wavelengths such that $\lambda < \lambda_0$, the fiber is said to exhibit normal dispersion. In normal dispersion regime, low frequency components of an optical pulse travel faster than high

frequency components of the same pulse. For $\beta_2<0$ (or $D>0$, i.e. for wavelengths such that $\lambda>\lambda_0$), the fiber displays anomalous dispersion, where in the high frequency components of an optical pulse travel faster than the low frequency components.

The dispersion and attenuation effects above assume that the light propagation in the fiber is in the linear regime. The next section discusses light propagation in the fiber, with fiber as a nonlinear medium.

2.4 Fiber Nonlinearities

Nonlinear effects in optical fibers occur mainly due to intensity dependence of the fiber refractive index and inelastic-scattering phenomenon. The stimulated Brillouin scattering (SBS) and stimulated Raman scattering (SRS) are the nonlinear scattering processes that arise due to the interaction of light waves with molecular vibrations in the silica medium. The nonlinear effects arising from intensity-dependent variations in refractive index in a silica fiber are SPM, CPM, and FWM. The presence of an optical field modifies the properties of the medium through third-order nonlinear susceptibility $\chi^{(3)}$, which in turn modifies the optical field travelling through it. A nonlinear dielectric medium is characterized by a nonlinear relationship between the polarization density P and the electric field E,

$$P = \varepsilon_0 \sum_{k=1}^{\infty} \chi^{(k)} E^k \tag{2.5}$$

Here ε_0 is the permittivity of free space and $\chi^{(k)}$ (k = 1, 2..) is the kth order susceptibility. The linear susceptibility is related to the dielectric constant and refractive index of the

material $n^2 = \varepsilon/\varepsilon_0 = 1+\chi$. The relation between P and E is linear when E is small, but becomes nonlinear when E acquires values comparable to inter-atomic electric fields, which are typically ~10^5 to 10^8 V/m [6]. For centro-symmetric media such as silica, the second-order nonlinear term is zero. The lowest order nonlinearity in such medium is of third order and the material is called a Kerr medium. For Kerr media, the refractive index is intensity dependent and the overall refractive index varies linearly with optical intensity I, $n(I) = n_0 + n_2 I$, where n_2 is the nonlinear index coefficient [6]. A figure of merit for the efficiency of the nonlinear process in single-mode fibers is given by the product of optical intensity I and the effective length of interaction L_{eff} [5]. The longer the fiber length, the more significant the light-matter interaction and thus greater the effects of nonlinearity. As the optical signal propagates in the fiber, its intensity decreases due to attenuation and accordingly, the nonlinear effects also diminish. To model this effect, as shown in Fig. 2.2, it is convenient to assume that the power is constant over a certain effective length L_{eff}.

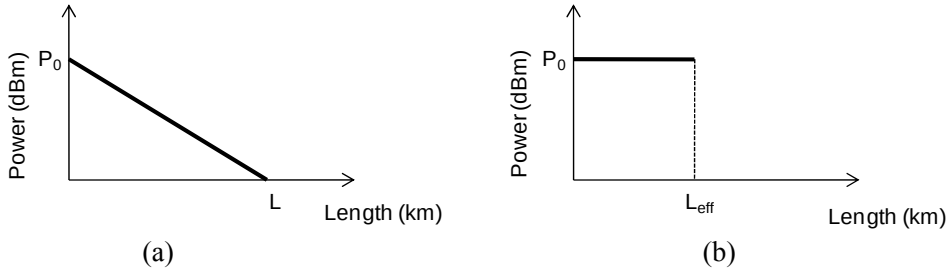

Fig. 2.2. Schematic diagram showing (a) a typical distribution of optical power along the length L of a link, (b) the effective length L_{eff} is modeled as the transmission length such that the area under the curve (on linear power scale) in (a) is equal to the area of the rectangle (on linear power scale) in (b).

The optical power $P(z)$ at a distance z along the link is given by $P(z) = P_{in}\, e^{-\alpha z}$, where P_{in} is the input power at $z = 0$ and α is coefficient of attenuation. For an actual link length L, the effective length L_{eff} is defined as [3],

$$P_{in} L_{eff} = \int_{z=0}^{L} P(z)dz \tag{2.6}$$

Using $P(z) = P_{in}\, e^{-\alpha z}$, in Eq. (2.6), we obtain,

$$L_{eff} = \frac{1 - e^{(-\alpha L)}}{\alpha} \tag{2.7}$$

In addition to the transmission length, nonlinear interaction also depends on the optical intensity. The effect of nonlinearity increases with the intensity in the fiber and decreases with increase in area of the fiber core, as $I = P / \pi w_0^2$, where P is the optical power and w_0 is the spot size of light in the fiber. For single-mode fibers, mode-field diameter (MFD) is a measure of the spot size or beam width of the light propagating in a fiber. Effective area of various types of fibers can be calculated using equation,

$$A_{eff} = \frac{\pi MFD^2}{4} \tag{2.8}$$

The effective area for the fundamental mode propagating in the standard single-mode fibers is about 80 μm^2 (MFD = 10 μm). As $I = P/A_{eff}$, most nonlinear effects are dependent on the effective area for the light propagating in the given type of fiber. The three nonlinear mechanisms that are mainly responsible for the signal distortion are SPM, CPM, and FWM. CPM and FWM are inter-channel nonlinearities present only in

WDM systems, while SPM is intra-channel nonlinearity and thus can occur even in single-channel systems.

2.4.1 Self-Phase-Modulation (SPM)

SPM arises because the refractive index of an optical fiber is intensity dependent [7],

$$n = n_0 + n_2 I = n_0 + n_2 \frac{P}{A_{eff}} \tag{2.9}$$

Here, n_0 is the linear part of refractive index, the quantity $n_2 = \frac{2}{\varepsilon_0 c n}\frac{3}{8n}\chi^{(3)}$ is the nonlinear refractive index coefficient and P is the instantaneous power of optical signal. In silica, the factor n_2 is about $2.6\text{x}10^{-20}$ m^2/W [8]. The nonlinear refractive index of silica converts intensity fluctuations into phase fluctuations [9]. The variations in the intensity of light produces change in the nonlinear refractive index, which in turn causes fluctuations in the phase. As the refractive index is intensity dependent, time varying signal intensity produces a time varying refractive index and as phase fluctuations are intensity dependent, different parts of the pulse undergo different phase shifts. Thus, SPM gives rise to intensity-dependent phase shift given by [5],

$$\Phi_{NL}(t) = \frac{n_2 2\pi L_{eff} P(t)}{A_{eff}\lambda} = \gamma L_{eff} P(t) \tag{2.10}$$

The nonlinear coefficient γ is defined as,

$$\gamma = \frac{n_2 2\pi}{A_{eff}\lambda} = \frac{n_2 \omega_0}{c A_{eff}} \tag{2.11}$$

The value of γ ranges from 1 to 30 $W^{-1}km^{-1}$ depending on the fiber type and wavelength [11]. The time dependence of Φ_{NL} is responsible for change in frequency spectrum, which is given by,

$$\delta\omega = -\frac{\partial \Phi_{NL}}{\partial t} = -\gamma L_{eff} \frac{dP}{dt} \tag{2.12}$$

This variation of phase with time gives rise to time dependence of δthe frequency shift δω, and is known as frequency chirping. This frequency chirping induced by SPM generates new frequency components and thus leads to spectral broadening of the pulse. The SPM-induced spectral broadening increases with Φ_{NL}, which in turn increases with the peak power P_0. The effect of SPM on an optical pulse as it propagates inside a fiber is shown Fig. 2.3. Since the nonlinear phase shift Φ_{NL} is intensity-dependent, the center (peak) of the pulse undergoes maximum phase shift, and the leading and the trailing edges of the pulse undergo smaller phase shifts. Also, as the frequency is the derivative of phase, the leading edge of the pulse (where Φ_{NL} increases) experiences a negative frequency shift or red-shift and the trailing edge of the pulse experiences a an up-shift or blue-shift in frequency (shifted towards higher frequencies or lower wavelengths).

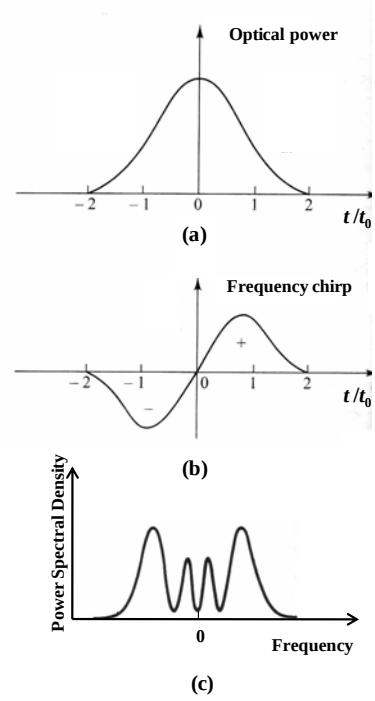

Fig. 2.3. Schematic diagram showing the effect of SPM for an unchirped Gaussian pulse (a) temporal variation of optical power, (b) derivative of pulse profile or frequency chirp, and (c) SPM-broadened spectrum.[((a) and (b) Revised from Fig. 12.8 in Ref. [10] and (c) Revised from Fig. 4.2 in Ref. [5]].

As seen in the Fig. 2.3, the SPM-induced chirp is linear and positive (chirp factor $\kappa > 0$) over a large central region of the pulse. In case of SPM, there is broadening of the spectrum without change in the temporal shape of the pulse. An initial chirp in the input pulse leads to qualitative changes in SPM-induced spectral broadening [5]. A positive chirp increases the SPM-induced spectral broadening, as (chirp factor $\kappa > 0$) over a large central region of the pulse. In case of SPM, there is broadening of the spectrum without change in the temporal shape of the pulse. An initial chirp in the input pulse leads to qualitative changes in SPM-induced spectral broadening [5]. A positive chirp increases the SPM-induced spectral broadening, as the

SPM-induced positive chirp adds with the initial chirp of the input pulse. For negative chirp, the two chirp contributions are of opposite signs and as a result, the pulse spectrum becomes narrower than that of initially unchirped pulses. SPM by itself leads to only chirping. The presence of the chirp significantly enhances the pulse broadening due to chromatic dispersion. Thus, when GVD and SPM act together, the SPM-induced chirp modifies the pulse broadening effects of dispersion depending on the sign of β_2. The effect of dispersion on SPM is studied in detail in section 3.1.

2.4.2 Cross-Phase-Modulation (CPM)

CPM arises because the refractive index of silica fibers is intensity-dependent. CPM occurs in WDM systems when two or more optical channels are transmitted simultaneously inside a single fiber. In such systems, CPM arises because the effective refractive index seen by an optical beam in a nonlinear medium depends not only on the intensity of that beam but also on the intensity of other copropagating beams [5]. As a result, when two or more channels propagate simultaneously, CPM converts power fluctuations in a particular channel to phase fluctuations in the other channels [9]. CPM is always accompanied by SPM. The nonlinear phase shift for channel *i*, is given by [7],

$$\Phi_i^{NL} = \gamma L_{eff}(P_i + 2\sum_{m \neq i} P_m) \tag{2.13}$$

Here, the first term is due to SPM (optical power P_i modifies its own phase Φ_i) and the second term due to CPM. As observed in Eq. (2.13), the nonlinear phase shift encountered by a specific channel depends not only on the power of that channel but also on the power of the other channels, and thus, this phenomenon is known as cross-

phase modulation. The factor of 2 in equation indicates that CPM is twice as effective as SPM for the same amount of power [7]. The total phase shift depends on the powers in all the channels and would vary from bit to bit depending on the bit pattern of the neighboring channels [7]. The CPM-induced phase shift or spectral broadening will not affect amplitude-modulated system if the GVD effects are negligible. Chromatic dispersion transforms this CPM-induced spectral broadening into amplitude- and timing-jitters. However, in presence of dispersion, pulses belonging to different channels travel at different speeds and walk through each other at a rate that depends on their wavelength separation. The walkoff length is defined as [8], $L_w = 1/(BD\Delta\lambda)$, where B is the bit rate, D the fiber chromatic dispersion, and $\Delta\lambda$ the channel separation. The CPM-induced phase shift can occur only when two pulses overlap in time and its impact is reduced considerably by the walkoff effects (i.e. CPM in Eq. (2.13) is determined by the walkoff length L_w rather than by effective length L_{eff}, with $L_w < L_{eff}$). For widely separated channels they overlap for such a short time that CPM effects are almost negligible. On the other hand, pulses in neighboring channels will overlap long enough for CPM effects to accumulate. As pulses in different channels propagate simultaneous in a fiber, the CPM-induced chirp shifts the pulse spectrum first toward red and then toward blue. Complete interaction of two pulses, i.e., when two pulses walk through each other completely, results in zero total phase shift. However, the amount of time the two pulses overlap causes delay and leads to timing jitter. The impact of CPM can be reduced by employing dispersion management techniques.

2.4.3 Four-Wave-Mixing (FWM)

FWM is a nonlinear process by which signals at different wavelengths are mixed together to produce new signals at new wavelengths. FWM has been recognized as one of the limiting factors in the design of high-performance WDM optical transmission links with a large number of channels [11]. FWM generates new wave at frequency $f_{ijk} = f_i + f_j - f_k$, whenever three waves at frequencies f_i, f_j, and f_k copropagate inside the fiber.

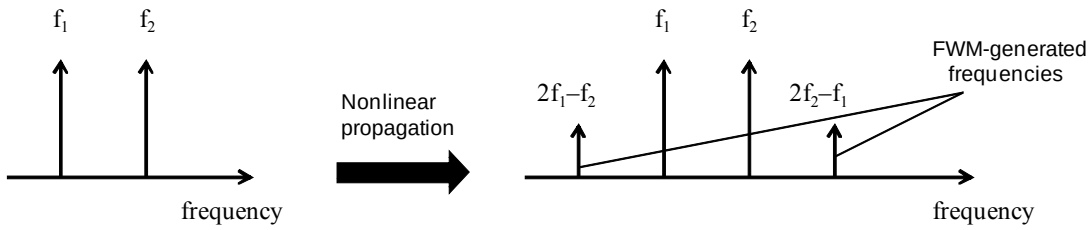

Fig. 2.4. Two optical waves at frequencies f_1 and f_2 mix to generate two sidebands at $2f_1$-f_2 and $2f_2$-$f\lambda_1$.

Figure 2.4 shows two channels at frequencies f_1 and f_2 generate, by FWM, two sidebands at $2f_1$- f_2 and $2f_2$- f_1. For an N channel system, the number of new products M generated by FWM is, $M = N^2$ (N-1)/2 [8]. In the case of equally spaced channels, the new frequencies coincide with the existing frequencies leading to in-band crosstalk. When channels are not equally spaced, most FWM generated components fall in between the channels and leads to crosstalk, which does not degrade the system performance as severely as in-band crosstalk. However, in both cases, in addition to the crosstalk interference, the depletion of the original signal waves can severely degrade multi-channel system performance. Assuming that the channels involved in the FWM

process remain undepleted, the peak power of the mixing product, generated at frequency f_{ijk}, after traversing a fiber of length L is [8],

$$P_{ijk} = \left(\frac{D_{ijk}}{3} \gamma L_{eff} \right)^2 P_i P_J P_k e^{-\alpha L} \eta \tag{2.14}$$

where D_{ijk} is the degeneracy factor, D_{ijk} =3 for two-tone products ($f_i = f_j$) and D_{ijk} = 6 for three-tone products ($f_i \neq f_j$) [8], and P_i, P_j, and P_k are the input peak powers of the channels at frequencies f_i, f_j, and f_k, respectively. The FWM efficiency η is defined as [8],

$$\eta = \frac{\alpha}{\alpha + \Delta\beta^2} \left(1 + \frac{4e^{-\alpha L} \sin^2(\Delta\beta L/2)}{(1 - e^{-\alpha l})^2} \right) \tag{2.15}$$

The quantity $\Delta\beta$ is the difference of the propagation constants of the various waves, due to dispersion, and is given by [8],

$$\Delta\beta = \beta_i + \beta_j - \beta_k - \beta_{ijk} = \frac{2\pi\lambda^2}{c}(f_i - f_k)(f_j - f_k)[D(\lambda)] - \frac{\lambda^2}{c}\left(\frac{f_o + f_j}{2} - f \right) \frac{dD}{d\lambda} \tag{2.16}$$

The efficiency of FWM depends on fiber dispersion and the channel spacing. For relatively large fiber chromatic dispersion, the FWM efficiency η nearly vanishes. In the case of equal channel powers ($P_i = P_j = P_k$ in Eq. 2.14), P_{ijk} scales with P^3. The cubic dependence of the peak power of the FWM generated component limits the channel powers to below 1 mW if FWM is nearly phase matched [7]. As FWM depends on phase-matching relationship between the interacting channels, in order to reduce the effects of FWM in WDM systems it is important to have a large value of GVD throughout the link. In presence of dispersion, the signals at different interacting

wavelengths travel with different phase velocities and, as a result, the newly generated mixing products are added in and out of phase with each other periodically with distance $L_{FWM} < L_{eff}$. This destroys the phase-matching condition of the interacting waves and minimizes the effects of FWM.

2.5 All-optical Regeneration

The capacity and reach of optical networks is limited by a combined effect of amplifier noise accumulation, chromatic and polarization-mode dispersion, fiber nonlinearity, inter-channel crosstalk, multipath interference, and other impairments. These degradations can be mitigated either by using conventional electronic regeneration, or by employing inline all-optical regeneration. As mentioned earlier, for multi-channel WDM systems electronic regeneration requires separate repeaters for each channel, thus increasing cost and complexity. All-optical regenerators are more attractive for high capacity networks, compared to OEO repeaters because of their capabilities of ultra-high-speed performance over 160 Gb/s [12] and simultaneous multi-channel processing. A 3R all-optical regenerator is a device that transforms the degraded bit stream into its original form by performing three functions: reamplification, reshaping, and retiming. The simplest type of optical regenerator is 1R, and performs only optical amplification function (e.g., an EDFA) . Another alternative is to use reshaping along with reamplification, but without retiming. Such type of regeneration is called as 2R regeneration. In all-optical regeneration, the signal is manipulated in optical domain, which requires the use of nonlinear materials. The nonlinear input-output response is the key parameter that governs regeneration efficiency and the highest regeneration

efficiency is achieved with step function (hard threshold). A variety of techniques have been used for practical implementation of optical regeneration using devices such as, saturable absorbers, nonlinear interferometer/gates, and synchronous modulators followed by nonlinear transmission fiber [13]. With introduction of HNLF and photonic crystal fiber/holey fiber, use of these fibers as nonlinear medium for signal regeneration has become very common. The key advantage of fiber devices lies in the near-instantaneous (femtoseconds) response of the Kerr nonlinearity, making them very attractive for ultra high bit rate operation (≥ 160 Gb/s) [13]. Many techniques have been developed for all-optical regeneration utilizing three major nonlinear effects: SPM [2], CPM [14], and FWM [15]. This section focuses mainly on SPM-based all-optical regenerators.

SPM-based regenerators can be divided into two categories based on the dispersion of HNLF. In the case of anomalous GVD, the SPM-based regenerator relies on the soliton-like pulse compression in the anomalous dispersion fiber and bandpass filtering, and is often referred as soliton-based regenerator [16, 17]. For HNLF with normal GVD, the SPM-based regenerator relies on spectrum broadening in normal dispersion fiber and subsequent spectrum slicing by OBPF [2]. In both cases, the device consists of an optical amplifier followed by an HNLF and an optical bandpass filter (Fig.2.5).

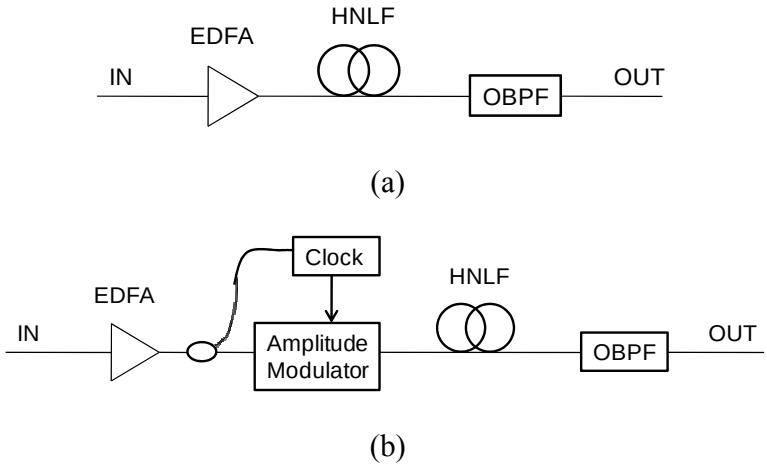

Fig. 2.5. An SPM-based optical signal regenerator: (a) 2R regenerator, (b) 3R regenerator. (Revised from Fig. 1 in Ref. [18]).

As seen in Fig. 2.5, in 3R regenerator the retiming function is generally added by placing a synchronous amplitude modulator in front of HNLF [18]. For soliton-based regenerator, the center frequency of OBPF is generally tuned to input carrier frequency. In the case of normal GVD, the center frequency of OBPF is offset from the carrier frequency. The regenerator based on spectrum broadening and slicing has a better ability to reduce noise and stabilize amplitude, compared to the soliton-based regenerator [18]. The fiber-based 2R regenerator [2], based on spectrum broadening and subsequent off-center filtering, has attracted particular attention because of its simplicity and robustness. In this scheme, the offset filter acts as a decision element. The offset is chosen such that the noise in the ZERO symbols is rejected at the filter due to insufficient spectral broadening of weak ZERO pulses, and the pulses representing ONE symbols pass though the filter without much distortion. When multiple channels propagate in the nonlinear medium, there is significant performance degradation as a

result of nonlinear inter-channel crosstalk due to CPM and FWM. Therefore, direct implementation of single channel regeneration techniques for simultaneous regeneration of multiple WDM channels is restricted by inter-channel nonlinearities.

In conventional transmission systems, several methods have been introduced for suppressing inter-channel crosstalk, out of which the most frequently employed are: using large effective area fibers, dispersion management, and polarization interleaving of adjacent channels. Dispersion management reduces FWM and CPM effects by using fiber sections with large dispersion and at the same time ensuring that the total accumulated dispersion returns to zero at the end of the system. Relative polarization of adjacent channels determines the strength of nonlinear interaction between them. The nonlinear crosstalk is the largest for channels with parallel relative state of polarization and smallest for the orthogonal case. For two channels launched into the fiber with orthogonal state of polarization FWM is negligible, while CPM is only half of the one in parallel case [19]. However, not all of these methods can be applied to inter-channel degradations in all-optical regenerators. Because, unlike the weakly nonlinear transmission systems, the regenerators are inherently highly nonlinear systems. So far, several schemes have been proposed and several attempts have been made to experimentally demonstrate simultaneous multi-channel all-optical regeneration. A dispersion-managed soliton-based regenerator was used to experimentally demonstrate simultaneous regeneration of 4x40 Gb/s channels [20]. This regenerator configuration used a periodic nonlinear fiber, achieved by periodic arrangement of combination of SMF and reverse dispersion fiber, instead of a conventional nonlinear fiber. Using fiber

sections with large dispersion, this configuration could suppress FWM effects. However, the strong CPM forced the use of polarization interleaving and limited the total number of regenerated channels to four. A multi-channel 2R regenerator scheme using a modified nonlinear amplifying loop mirror (NALM) is proposed in Ref. [21]. Using this configuration, simultaneous regeneration of 2x10 Gb/s channels using differential phase-shift-keyed (DPSK) modulation format was experimentally demonstrated. However, in order to prevent the XPM and FWM effects during multi-channel regeneration, this regenerator used separate nonlinear fibers for each WDM channel and thus increased the complexity of the setup. In addition, a strong crosstalk between neighboring channels in the multiplexers forced a large spectral spacing of 1100 GHz between the channels. In [22], an SPM-based 2R regeneration scheme in a bi-directional configuration is proposed and simultaneous regeneration of 2 x 10 Gb/s is experimentally demonstrated. This bidirectional configuration, in which two channels propagated within the same fiber but in opposite directions, was able to suppress the inter-channel crosstalk due to FWM and CPM. However, the presence of Rayleigh backscattering limits the multi-channel operation of the regenerator. Two more four-channel regeneration experiments employed a combination of polarization multiplexing and bi-directional propagation [23] and very low duty cycle pulses combined with low spectral efficiency (600 GHz spacing with 10 Gb/s) [24] to avoid inter-channel interactions.

Thus, the above mentioned approaches cannot be used for simultaneous all-optical regeneration of a large number of WDM channels. The next chapter explains the

concept of our proposed multi-channel all-optical 2R regenerator that can be scaled to large WDM channel count.

CHAPTER 3

CONCEPT OF MULTI-CHANNEL ALL-OPTICAL 2R REGENERATION

Our proposed multi-channel 2R regenerator comprises multiple unit sections consisting of HNLF and PGDD. HNLF, with high normal dispersion, is used as a nonlinear medium to achieve all-optical regeneration and PGDD is employed for dispersion compensation. This chapter focuses on two key factors that govern the working of our regenerator, SPM in HNLF and dispersion management using PGDD. The effects of GVD on SPM are discussed in section 3.1. Section 3.2 describes dispersion compensation using PGDD. The last section of this chapter explains the concept our proposed multi-channel all-optical 2R regenerator.

3.1 Self-Phase-Modulation (SPM) in Highly Nonlinear Fiber (HNLF)

As mentioned in the Section 2.4, the cause for SPM in single-mode fibers is the intensity-dependence of the refractive index. For HNLF with large fiber dispersion, when the pulses become shorter, the dispersion length L_D becomes comparable to nonlinear length L_{NL}. As a result, it becomes necessary to consider the combined effects of SPM and GVD. For pulse widths greater than 5 ps, the nonlinear Schrodinger (NLS) equation that governs propagation of optical pulses inside single-mode fibers is given by [5],

$$i\frac{\partial A}{\partial z} = -\frac{i\alpha}{2}A + \frac{\beta_2}{2}\frac{\partial^2 A}{\partial T^2} - \gamma|A|^2 A \tag{3.1}$$

where A is the slowly varying amplitude of the pulse envelope and T is measured in a frame of reference moving with the pulse at the group velocity v_g ($T = t - z/v_g$) [5]. The first two terms on the right-hand side govern the linear effects in the optical fiber: fiber losses through α ($P(z) = P(0)\, e^{-\alpha z}$) and GVD through β_2. The third term includes the effects of nonlinearity on the pulses propagating inside optical fibers through nonlinear parameter γ. The initial width T_0 and the peak power P_0 of the incident pulse determine whether the dispersive or nonlinear effects would dominate along the fiber. The dispersion length L_D and the nonlinear length L_{NL} provide the length scales over which dispersion or nonlinear effects become important for pulse evolution and are given by [5],

$$L_D = \frac{T_0^2}{|\beta_2|}, L_{NL} = \frac{1}{\gamma P_0}, \tag{3.2}$$

$$N^2 = \frac{L_D}{L_{NL}} \equiv \frac{\gamma P_0 T_0^2}{|\beta_2|}. \tag{3.3}$$

When $L << L_{NL}$ but $L \sim L_D$, i.e. $N << 1$, GVD dominates over SPM that leads to temporal broadening of the pulse. Thus, for dispersion-dominant regime [5],

$$N = \frac{L_D}{L_{NL}} = \frac{\gamma P_0 T_0^2}{|\beta_2|} << 1. \tag{3.4}$$

When the width and the peak power of the input pulse are such that $L_D >> L > L_{NL}$, the GVD effects are negligible and the pulse propagation in the fiber is governed by SPM which leads to spectral broadening of the pulse. The nonlinearity-dominant regime is applicable whenever,

$$N = \frac{L_D}{L_{NL}} = \frac{\gamma P_0 T_0^2}{|\beta_2|} >> 1. \tag{3.5}$$

When the fiber length is longer or comparable to both L_D and L_{NL} (N~1), dispersion and nonlinearity act together as the pulse propagates along the fiber. In case of SPM alone, there is broadening of the spectrum, but the temporal shape of the pulse remains unchanged. In case of dispersion alone, there is broadening of the pulse in time domain, while the spectral contents are unaltered. The interplay of GVD and SPM effects can lead to a qualitatively different behavior compared with that expected from GVD or SPM alone. The combined effect of GVD and SPM is different for pulses propagating in the normal-dispersion regime ($\beta_2>0$) and for anomalous-dispersion regime ($\beta_2<0$). As explained earlier, SPM generates new frequency components that are red-shifted near the leading edge and blue-shifted near the trailing edge of the pulse. For normal dispersion fiber ($\beta_2<0$), red components travel faster and blue components travel slower. When the SPM-affected pulse travels within the fiber with normal dispersion, the red components continue to travel faster and the blue components continue to travel slower and thus both components move away from the center of the pulse. Therefore, in normal dispersion regime, SPM worsens dispersion-induced temporal pulse broadening. This in turn affects spectral broadening as the SPM-induced phase shift Φ_{NL} becomes less than that occurring if the pulse shape were to remain unchanged [5]. In anomalous dispersion regime ($\beta_2<0$), red components travel slower and blue components travel faster. When the SPM affected pulse travels within the fiber with anomalous dispersion, the red components travel slower and move towards the center of the pulse. Also, the blue

components continue to travel faster and move towards the center of the pulse. This is because the SPM-induced chirp (positive) and the dispersion-induced chirp (negative) are opposite in signs for $\beta_2 < 0$ and the two chirp contributions nearly cancel out each other when N=1(soliton regime) [5]. For N>1, when propagating in the anomalous dispersion regime of the fiber, the pulse may drastically narrow leading to explosion in the spectral width. To summarize, the SPM and GVD, in general, can not be treated separately, and their combined effect may lead to complicated evolution of the signal in both time and frequency domain.

3.2 Dispersion Compensation

Dispersion compensation consists of combining fibers with different characteristics such that the average GVD of the entire link is quite low while the GVD of each fiber section is chosen to be large enough to make the FWM effects negligible and XPM effects small [7,8, 25]. This can be accomplished by combining two kinds of fibers, with opposite signs of β_2, so that the average dispersion is reduced to a small value. If L_1 and L_2 are the lengths of fiber segments one and two respectively, and D_1 and D_2 their respective dispersion parameters, then the condition for 100% dispersion compensation can be given as [5]:

$$D_1L_1 + D_2L_2 = 0 \,. \tag{3.6}$$

If $L_1 = L_2$, i.e. if two segments are of equal lengths, the fibers should have opposite dispersions, i.e. $D_1 = -D_2$, in order to satisfy equation (3.6). DCF exhibiting a large positive value of β_2 (large negative value of D) is commonly used for compensating large accumulated dispersions in SSMFs and NZDSFs. With 100 km

SSMF (D~ 17 ps/nm/km) employed as the transmission fiber, only 17 km of DCF (D ~ −100 ps/nm/km) is required for dispersion compensation. DCF has a much narrower core and relatively high attenuation (α=0.5 dB/km) in the 1.55 μm wavelength region. The greater the length of the transmission fiber, the longer will be the required length of DCF in order to compensate the dispersion induced by the transmission fiber. As a result, the DCF-based dispersion compensating modules become bulky and have high insertion loss. In single-span systems, dispersion compensation is performed by placing the DCF near the transmitter or the receiver. However, in multi-span systems dispersion compensation is commonly performed by placing DCF at the inline amplifier site (typically, between two stages of the amplifier) to achieve periodic dispersion compensation along the transmission link. Since DCF fibers are more susceptible to nonlinear effects because of their lower effective areas, the signal power level from the first stage should not be high. This limits the use of DCF to places where the signal power is relatively low. The dispersion of optical transmission fiber varies significantly over the C-band, because of the dispersion slope ($dD/d\lambda > 0$). This wavelength dependence of the chromatic dispersion becomes important in WDM systems because different wavelengths need different dispersion compensation. As a result, compensation of dispersion slope becomes necessary. When DCF with zero or positive slope ($dD/d\lambda \geq 0$) is used to compensate the dispersion of transmission fiber, different wavelengths will have different amount of residual dispersion. Therefore, only one channel is completely compensated while the channels away from that wavelength will

be either under- or over-compensated for dispersion. Newer DCFs are designed with $dD/d\lambda < 0$ to mitigate this effect (dispersion-slope compensation).

Another technique to compensate the accumulated dispersion of the transmission fiber is to use fiber Bragg gratings (FBGs). FBG-based dispersion compensators provide an attractive alternative to dispersion compensation without some of the associated drawbacks of conventional DCF-based dispersion compensating modules. In [26], a 32-channel dispersion compensator with 100 GHz spacing designed for the compensation of 50 km of SMF using a single 32-component grating has been demonstrated. The insertion loss of this 32-channel dispersion compensator is reported to be less than 2.2 dB. This insertion loss is significantly lower than the one obtained with DCF and is independent on the dispersion level, which makes FBG-based dispersion compensators even more attractive for higher dispersion levels [26]. For long-haul WDM systems at 10 Gb/s, multi-channel tunable dispersion compensation is now necessary. Further, at transmission rates of 40 Gb/s and above, slope matching and dynamically tunable dispersion compensation will be required [27]. Thermally tuned chirped FBG is well suited and readily adapted to dispersion compensation in single- or multi-channel systems [26].

3.2.1 Dispersion Compensation using PGDD

An FBG is an optical fiber, whose refractive index is periodically modulated over a certain length. The light is reflected when its wavelength is equal to the Bragg wavelength $\lambda_B = 2n_{eff}\Lambda$, where n is the effective refractive index of the fiber and Λ is the period of grating. Therefore, when several wavelengths are transmitted into a FBG, the

Bragg wavelength is reflected while the other wavelengths are transmitted. A FBG used as a dispersion compensator, the grating period is reduced linearly along the length of the fiber (chirped FBG), due to which the Bragg wavelength decreases with distance along the grating length. As a result, the high frequency components (shorter wavelength) experience more delay in going through the grating than the longer-wavelength components. The relative delays induced by the grating on the different frequency components of the pulse are the opposite of the delays caused by the transmission fiber and thus the FBG dispersion compensator compresses the pulse. The dispersion introduced by the grating corresponds to variation of group delay as a function of wavelength. A single-channel dispersion compensator is fabricated by writing a single grating in an optical fiber. A periodic group delay device (PGDD), that has a group delay that repeats itself periodically, is required for simultaneous dispersion compensation of multiple WDM channels. A multi-channel dispersion compensator can be made by writing many CFBGs in separate sections of a fiber [28].Some of the CFBG-based techniques used to achieve multi-channel dispersion compensation are, fabrication of ultra-long CFBGs, fabrication of sampled CFBGs, and superposition of multiple CFBGs [26]. Superimposing multiple CFBGs on the same section of fiber allows packaging of multiple gratings in one package, thus minimizing device dimensions [26, 28]. Using a multi-channel CFBG based on grating superposition, dispersion compensation over up to 32 channels has been achieved [FBG and CD]. By combining superimposed multiple CFBGs along with a thermal gradient tuning platform, a multi-channel tunable dispersion compensator has been fabricated [26].

The dispersion of FBGs can be varied by using a temperature gradient. The temperature profile is achieved by using two thermo-electric coolers (TECs) and a heater, which also minimizes the impact of external temperature fluctuations. Depending on its sign, the temperature gradient causes an increase or a decrease of the dispersion [29]. A dual-grating configuration (Fig. 3.1) provides a dispersion tuning range around 0 ps/nm [30].

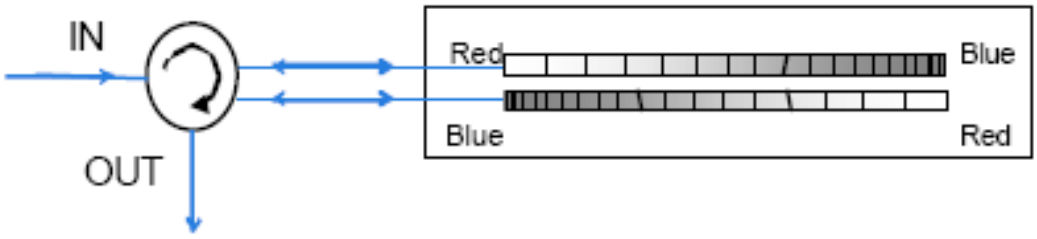

Fig. 3.1. Schematic of the dual-grating configuration to achieve dispersion tuning range around 0 ps/nm [29].

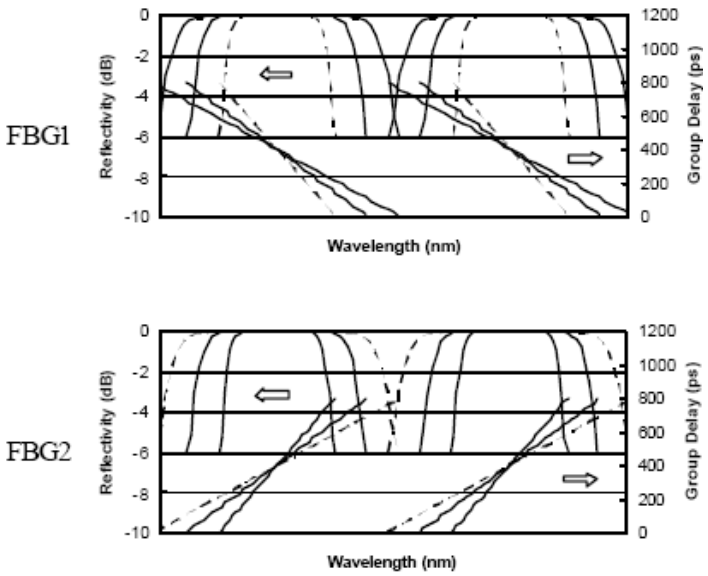

Fig. 3.2. Reflectivity and group delay spectra shown over two channels for two FBGs located in the same thermal platform without thermal gradient (thick solid line) and with positive (dashed line) and negative (thin solid line) thermal gradients [31].

The two gratings of opposite chirps are placed in the same thermal platform that imposes the temperature gradient. As seen in Fig. 3.2, when a negative temperature gradient is applied, it causes a decrease of the dispersion magnitude of a negative dispersion grating (FBG1 in Fig. 3.2) and an increase of the dispersion for a positive dispersion grating (FBG2 in Fig. 3.2). When these two FBGs are connected to a 4-port optical circulator, their overall dispersion is the sum of the FBGs individual dispersion [31]. In an isothermal condition, the overall dispersion of the device is zero [30].

The channel bandwidth changes as the dispersion is tuned. For a given group delay range, the dispersion is obtained by the ratio of the group delay range and the channel passband [31]. The maximum dispersion is limited by channel narrowing while the minimum dispersion is restricted by crosstalk due to interference between adjacent channels.

3.3 Concept of our proposed multi-channel 2R regenerator

Our proposed 2R regenerator scheme [1], is a modified version of Mamyshev's single channel 2R regenerator [2]. In the original scheme proposed by Mamyshev (Fig. 3.3), an input pulse undergoes spectral broadening due to self-phase modulation (SPM) in a highly nonlinear fiber (HNLF). It is subsequently passed though a bandpass filter, whose center wavelength is shifted with respect to the input signal frequency.

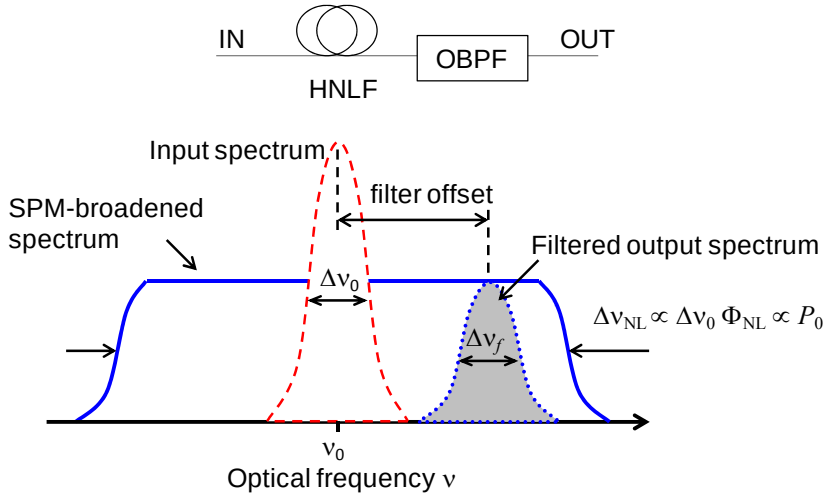

Fig. 3.3. Schematic diagram of Mamyshev's single channel 2R regenerator (top) and its operating principle (bottom).

If an input pulse has a full width half maximum (FWHM) spectral bandwidth of $\Delta\nu_0$, its spectrum is broadened to width $\Delta\nu_{NL}$, given by,

$$\Delta\nu_{NL} = \Delta\nu_0 \gamma P_0 L_{eff} = \Delta\nu_0 \frac{2\pi}{\lambda}\frac{n_2}{A_{eff}} P_0 L_{eff} \tag{3.7}$$

where P_0 is the input pulse peak power, n_2 is the nonlinear refractive index, A_{eff} is the effective area of HNLF, and L_{eff} is the effective length of HNLF. The peak power of output pulse after spectral filtering is proportional to the output spectral density ($P_0/\Delta\nu_{NL}$) [2]. For large input power when $\Delta\nu_{NL} >> \Delta\nu_0$, the output spectral density and, therefore, the power of output pulses becomes almost independent of the input power P_0. As a result, fluctuations of the input peak power translate into fluctuations of the width of the broadened spectrum, while the height of the spectrum remains constant. An optical band-pass filter (OBPF), shifted in frequency from the original signal carves out a portion of this constant-height broadened spectrum, creating output pulses with

stabilized magnitude which yields regeneration of ONE symbols. At the same time, noise in ZERO symbols, due to its small power, undergoes linear propagation without spectral broadening and is, therefore, rejected by the off-centered filter, producing regeneration of ZERO symbols.

The strong nonlinearity that enables single-channel regeneration degrades the multi-channel operation, as the channels will strongly interact with each other in HNLF and thus degrade the performance of regenerator. As a result, this regenerator configuration will not work for simultaneous regeneration of multiple WDM channels. Fig. 3.4 shows our proposed scheme for multi-channel 2R regenerator, in which the conventional HNLF is replaced by a novel artificial nonlinear medium. Instead of having one long section of HNLF, we break it into several short sections and separate them by Periodic Group Delay Devices (PGDDs).

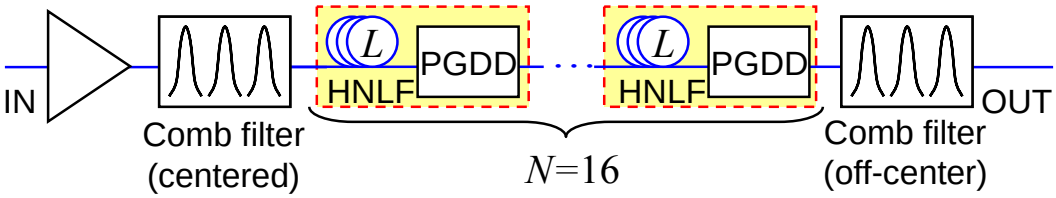

Fig. 3.4. Schematic of the proposed multichannel dispersion-managed regenerator.

The regenerator configuration consists of an EDFA, followed by periodic optical band pass filter (OBPF1), 16 identical HNLF-PGDD unit cells, and the OBPF2 at the end. The OBPF1, the center wavelength of which is fixed at the input signal's center wavelength, is used to remove the out-of-band ASE emitted from the EDFA. An initially unchirped pulse is amplified by EDFA and then injected into the HNLF. The

HNLF has high normal dispersion and as a result, due to the interplay of GVD and SPM, the pulse at the output of HNLF is broadened in both frequency and time domains. The PGDD, with large anomalous dispersion, compensates for the dispersion of HNLF. As the pulse propagates through PGDD, its temporal shape is restored while its spectral contents remains unaltered. At the output of the last PGDD, the pulse with SPM-induced chirp is filtered by the following periodic OBPF2, the center wavelength of which is offset with respect to the input signal's wavelength.

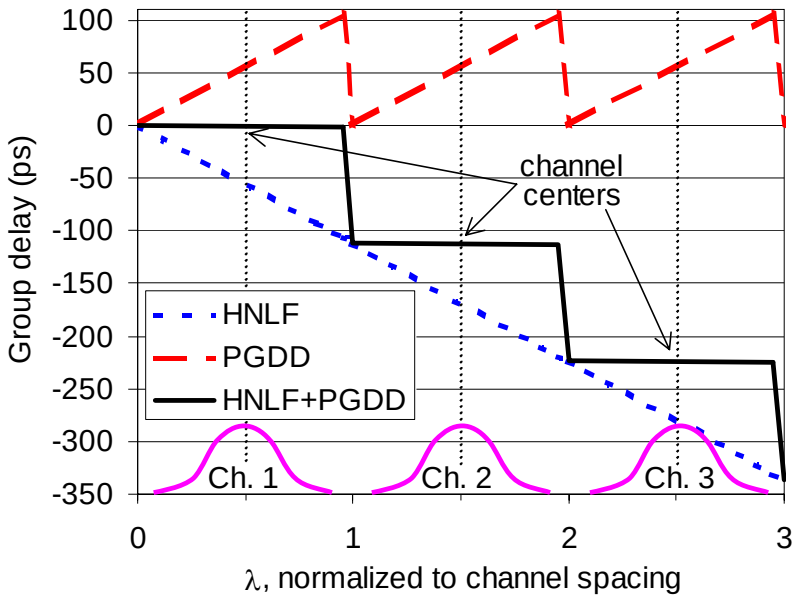

Fig. 3.5. Group delay of the HNLF, PGDD, and a single section of HNLF-PGDD.

PGDD is a key component of our proposed regenerator and has a periodic saw-tooth like group-delay spectrum (Fig. 3.5). The high local dispersion of HNLF enables pulses of neighboring channels to walk-off from each other. The combination of a piece of HNLF and PGDD forms one dispersion managed section and has a staircase like

group-delay spectrum, as seen in Fig. 3.5. As a result, the dispersion within each channel's band is kept small while the accumulated dispersion between the channels is high. With this dispersion map, different channels propagate with very different group velocities thereby suppressing inter-channel nonlinear effects (FWM and CPM) and, at the same time, various frequency components within each channel's bandwidth travel at same velocity (no change in pulse shape) ensuring sufficient SPM-induced spectral broadening. Concatenation of many PGDD-HNLF cells further increases the SPM spectral broadening while keeping the fast walk-off among the channels. At the same time, a low value of intra-channel dispersion is maintained.

The idea of using combination of fiber dispersion and PGDD to reduce FWM and CPM was introduced for weakly nonlinear conventional communication systems in [32, 33] and later applied to (again, weakly nonlinear) dispersion-managed soliton (DMS) transmission [34, 35].

In our regenerator, however, the regime of operation is drastically different from the conventional or DMS transmission systems: in the regenerator the high nonlinearity dominates over the dispersion. Therefore, the results of the prior studies [32-35] are not applicable here and a separate investigation of multi-channel all-optical regeneration is required.

The next chapter describes in detail the experimental set up and results of single- and multi-channel 2R regeneration using a recirculating loop testbed.

CHAPTER 4

EXPERIMENTAL SETUP AND RESULTS

4.1 Single-channel 2R Regenerator

As explained in previous chapter, our proposed multi-channel 2R regenerator is a modified version of Mamyshev's single-channel 2R regenerator. For practical realization of such a multi-channel 2R regenerator, we need to first experimentally show that our proposed dispersion-managed scheme does not adversely affect single-channel regeneration. This would prove that for single-channel, our dispersion-managed multi-channel 2R regenerator with HNLF-PGDD section functions just like the conventional SPM-based 2R generator with HNLF. For this task, we have built a recirculating loop setup shown in Fig. 4.1. The recirculating loop enables characterization of long-haul systems by putting a few components and a limited length of fiber in a loop and letting the signal propagate through them many times. In single-channel 2R regenerator, a section of HNLF is implemented by a 500-m-long piece of dispersion compensating fiber (DCF) with nonlinear constant $\gamma \sim 5\ W^{-1}km^{-1}$ and dispersion D= −120 ps/nm/km. In the single-channel case, we do not need the periodicity of PGDD response and for dispersion compensation we use a combination of standard single-mode fiber (SSMF) and non-zero dispersion-shifted fiber (NZDSF).

4.1.1 Experimental Setup

Figure 4.1 shows the schematic of single-channel experiment using a recirculating loop setup. The recirculating loop consists of four basic elements: transmitter, loop switch controller, transmission link, and receiver.

1. *Transmitter* contains two distributed feedback (DFB) lasers, a 70/30 coupler, polarization controller (PC), modulator, and an erbium-doped amplifier (EDFA). DFB lasers are used for their very narrow linewidth, and low relative intensity noise. The external modulator is a dual-stage $LiNbO_3$ Interferometric Mach-Zehnder Modulator (MZM). To compensate for the losses of modulator, PC, and coupler, we use an EDFA.

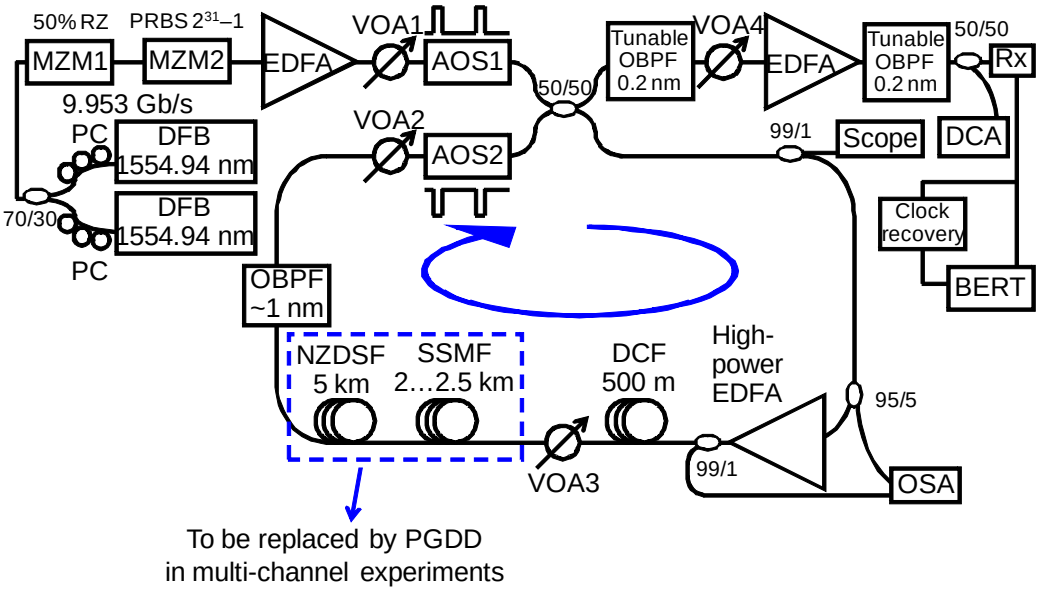

Fig. 4.1. Recirculating loop setup for single-channel 2R regeneration.

2. *Loop switch controller* is the most important active component in a recirculating loop. It acts as an optical switch, as it allows the data to either flow into the loop (the load state) or to circulate in the loop (the loop state). Loop Switch Controller mainly comprises of two acousto-optic switches (AOSs) and a 3-dB coupler. The AOSs are the essential elements in the loop switch and work in counter-phase, i.e. when AOS 1 is in "on" state (i.e. transparent) to load the loop, AOS 2 is in the "off" state (no light propagates through it), and vice versa. When AOS 1 is open ("on" state), signal enters 3-dB coupler, from which half of the signal goes to the receiver and the other half goes into the recirculating loop. By the time the signal reaches the end of the loop, AOS 1 closes and AOS 2 opens, and the signal circulates in the loop for as long as AOS 2 is open. Even though the AOSs are designed to be polarization-insensitive, they still exhibit some polarization-dependent loss (about 0.2 dB). To prevent accumulation of this loss over many circulations, we employ polarization controllers inside and outside the loop. Two SRS digital delay/pulse generators are used to trigger AOSs, receiver, Optical Spectrum Analyzer (OSA) and the Digital Communications Analyzer (DCA) simultaneously.
3. The transmission link of our loop contains one high-power erbium-doped fiber amplifier EDFA, a variable optical attenuator (VOA) VOA3, optical bandpass filter, 0.5 km of DCF, 2…2.5 km of SSMF (Corning SMF-28e^{TM}), and 5 km of NZDSF (Corning LEAF^{TM}). The combination of SMF and LEAF is used to

compensate the dispersion of 0.5 km of DCF so that the residual dispersion of one loop is in -5 to +5 ps/nm range. The 1-nm-wide OBPF (full-width at 1 dB is 0.65nm, full-width at -16 dB is 1.6 nm) is employed to suppress accumulation of out-of band ASE noise. The 5% and 1% taps are used in the loop to monitor the signal spectrum before and after amplification, at any given circulation on a Optical Spectrum Analyzer (OSA). The high power EDFA is placed at the beginning of the loop to boost the signal before launching it in DCF, to achieve SPM-induced spectral broadening essential for 2R regeneration. The variable optical attenuators, VOA1 and VOA2, are used to balance gain and loss after each round-trip so that the total signal powers after each round-trip are the same. This balance operation eliminates the wild transients of EDFAs that can damage the optical components in the loop.

4. *Receiver* continuously receives data from every circulation from the 3-dB coupler. The error detector connected to the receiver operates in the burst mode gated by the digital delay / pulse generator in order to detect the errors occurring after a particular number of circulations. The error detector compares the bits received during the gating period with the bits supplied to the transmitter by the pattern generator. Any difference between the patterns represents the bit error.

The setup operates as follows. Light from the DFB laser at 1554.94 nm is carved into 50% RZ pulses and modulated (modulator extinction ration of 13 dB) by 10 Gb/s, 2^{31}-1 pseudo random bit sequence (PRBS) pattern. The input signal is artificially

degraded by adding a small amount of light from a second independent co-polarized DFB source tuned to the same wavelength. The relative phase between the two DFBs fluctuates at a rate comparable to the DFB linewidth (~ 3MHz), leading to interference noise on the signal (coherent crosstalk). After amplification, signal is injected into the loop by acousto-optic switch AOS 1. Signal enters DCF from high-power EDFA, with average power always maintained near 60 mW (peak power of 250 mW). After DCF, VOA3 attenuates signal power into SMF and NZDSF to minimize nonlinear processes in these fibers. After a number of circulations through the loop, the signal is filtered by two cascaded 0.2-nm-wide tunable filters (cumulative FWHM= 20GHz) and detected by optically pre-amplified receiver. The tunable filters are both either on- centered (input signal measurement) or off-centered (regenerated signal measurement) with respect to the input signal's center wavelength. By using a measurement gating window coinciding with timing of a particular circulation in the loop, we can select the data to be acquired by the optical spectrum analyzer (OSA, Ando 6317B), bit error rate tester (BERT, Agilent 70843B) and digital communication analyzer (DCA, Agilent 83480A with 83485B plug-in and enhanced trigger option 100).

4.1.2 Triggering Setup

Two Stanford Research Systems (SRS) DG535 delay/pulse generators, termed SRS 1 and SRS 2 are used to trigger AOSs, receiver, Optical Spectrum Analyzer (OSA) and the Digital Communications Analyzer (DCA) simultaneously. Both generators have five delay output ports: T_0, A, B, C, D and four pulse outputs AB, −AB (i.e. inverted AB), CD, and −CD. The T_0 pulse marks the beginning of a timing cycle and is generated by

the trigger signal. The delays for each channel are either linked to T_0 or any of the other channels. High-Z termination needs to be set on SRS 1 and SRS 2 for all TTL signals.

Figure 4.2 shows trigger connections between these devices. SRS 1 controls AOS 1 and AOS 2, as well as the error detector (we typically do not use electrical gating of the DCA because it has performed very poorly, despite the presence of enhanced trigger option in the DCA). SRS 2 is externally triggered by −CD output on SRS1 and controls diagnostic devices, OSA and slow oscilloscope, and also performs fast optical gating of the OSA and the DCA. The input trigger on SRS 2 is set to 50Ω, with a threshold of +1.0 V and a negative slope. The AB output on SRS 1 is connected to the RF driver which drives AOS 1. Since the pulse that drives AOS 2 is the complementary to the pulse that drives AOS 1, AOS2 driver is connected to −AB (i.e. inverted) output on SRS 1.

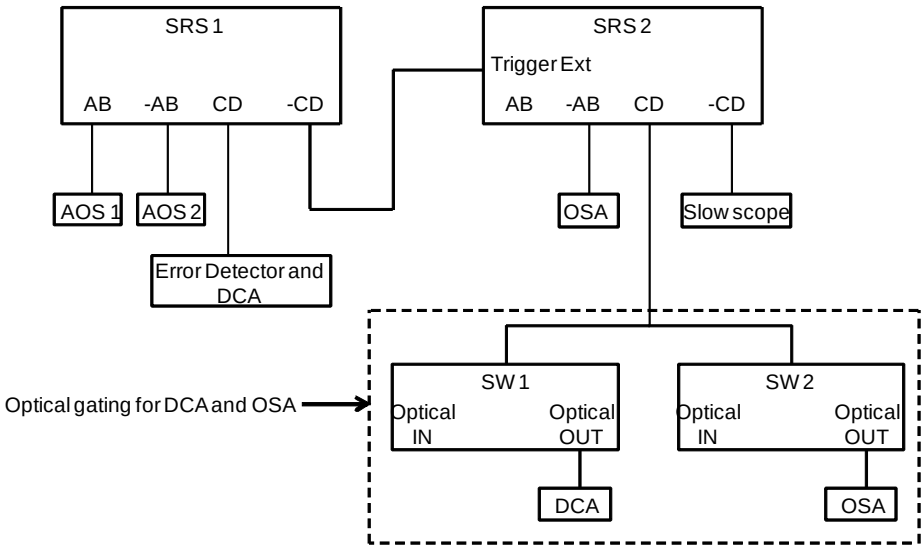

Fig. 4.2. Schematic showing connections between SRS delay / pulse generators 1 and 2 to other equipments of the setup.

The total length of fiber in the loop (DCF + SSMF + NZDSF), L_{total} is about 8 km. Using $T_{\text{circ}} = \frac{L_{\text{total}}}{c_g}$, where c_g is the group velocity of light in fiber, we obtain circulation time of 40 μs. The circulation time is the time taken by the signal to travel once around the loop. The time of the loading state (AOS 1 ON) must be equal to or greater than one circulation of the loop in order to allow the loop to fully fill up and ensure that the EDFAs are saturated and in steady state. As a result, the loading-state time, T_{load}, was set to 70 μs. This repetition rate is calculated by $R_{\text{rep}} = \frac{1}{T_{\text{load}} + T_{\text{loop}}}$, where $T_{\text{loop}} = m \times T_{\text{circ}}$ and m is the number of times the bit stream circulates in the loop before the loop is reloaded. Our simulation results show that for multi-channel 2R regeneration the required length of DCF is 7.5 km. Thus, with 0.5 km of DCF in the loop, the number of circulations m is set to 15. This results in loop time (T_{loop}) of 600 μs and a repetition rate of 1493 Hz. This calculated R_{rep} is set in the trigger menu of SRS 1. Table 1 lists the settings for the delay outputs of each generator.

Table 4.1. Delay settings of SRS 1 and SRS 2.

Delay Outputs	SRS 1	SRS2
A	T_0 + 10 μs	T_0 + 20 μs
B	A + 70 μs	T_0 + 10 μs
C	B - 40 μs (N=0)	T_0
D	C + 10 μs	C + 10 μs

The delay of channel B is linked to channel A with an added time of 70 μs, which is T_{load}. The output D is linked to C with an additional delay of 20 μs. The output pulse CD, which is equal to the time interval between channel C and channel D, is the gating pulse and has a pulse width of 20 μs. Adjusting the delay of D will change the width of the gating pulse. The width of the gating pulse must be smaller than T_{circ} to avoid any transients during the measurement time. The delay of output C is varied to move the gating pulse to a given circulation. The gating pulse is located not far from the center of T_{load} when delay of output channel C is B - 40 μs. Increasing delay of C will move gating pulse though increasing number of circulations. By adding 560 μs of delay to C (i.e. C = B + 560 μs) moves the gate to the center of circulation#15.

The measurement window corresponding in time to a particular circulation is selected by gating the DCA (fast oscilloscope), error detector, and OSA. The Agilent DCA specifies gating width of 1 μs at 10 GHz. The gating pulse input at least 1 μs long is supplied by SRS 1 using the CD output. The same signal is also used to gate the error detector. Despite having option 100 (enhanced trigger), our DCA has shown very poor timing-jitter performance in gated trigger mode. Therefore, we use another AOS (SW 1 in Fig. 4.2) to optically gate the input signal to the continuously triggered DCA. Gating input of the OSA (EXT TRIG IN) needs a negative-logic TTL signal, hence −AB (10 μs pulse width) on SRS 2 is used trigger it. The OSA gating pulse must be at least 5 μs long. In addition, we have found that the OSA essentially integrates the signal over 120 μs preceding the gate. Thus, to show the true spectrum after a particular circulation, longer loop length (propagation time longer than 120 μs) is needed. However, in multi-

channel experiments the loop length is very short, as the total length of fiber used in the loop is only about 1.25 km. As a result, to monitor the real spectrum of a given circulation, the OSA input is optically gated using another AOS (SW 2 in Fig. 4.2).

4.1.3 Results

Total dispersion of one loop was varied from -5 to +5 ps/nm, and we found that +5 ps/nm is the optimum value for best single-channel regeneration results. Figure 4.3 shows the signal spectra after *N* circulations through the loop. As the signal propagates through increasing number of circulations, we observe that the spectrum broadens and flattens at the top, which is similar to the conventional 2R regenerator with constant dispersion.

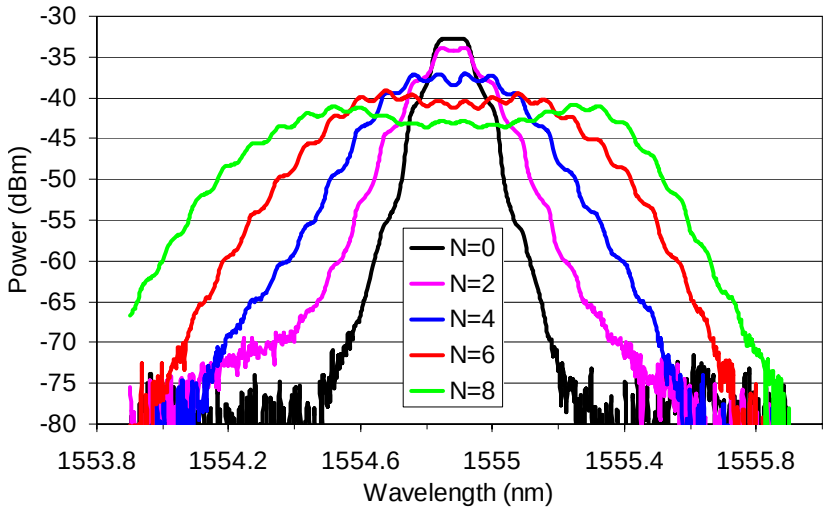

Fig. 4.3. Signal spectra after various numbers *N* of circulations.

One of the advantages of using a recirculating loop is that it allows us to monitor the signal degradations as the signal propagates along the regenerator. Figure 4.4 shows the eye diagrams of input and the output signal after circulations #2, #4,…, and #15 for

the optimum values of +5 ps/nm residual dispersion per loop and +0.25 nm detuning of the tunable filters from the input signal's center wavelength. In Fig. 4.4 we can see that as the number of circulations increase, the spectral broadening increases and, the sliced portion of spectrum has a better content of the output signal.

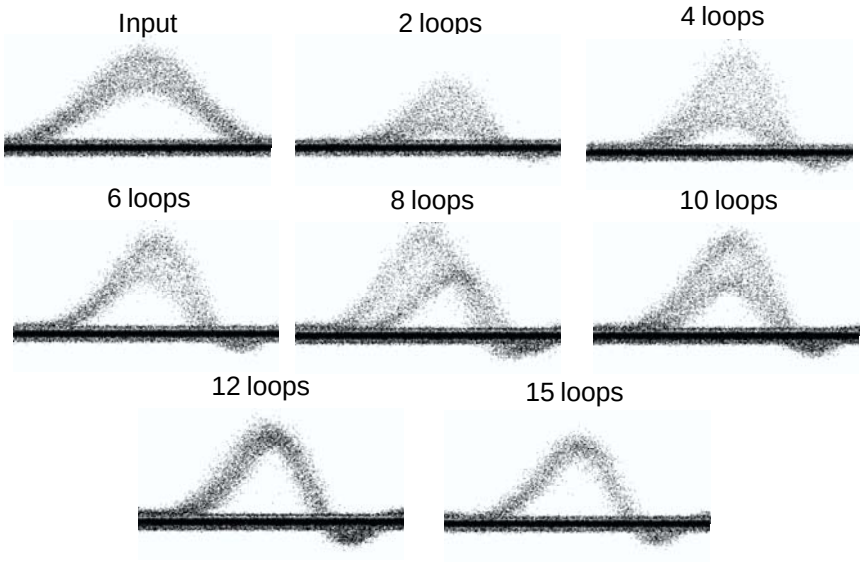

Fig. 4.4. Eyes for signal input (after 0 circulations, no detuning) and output (after 2…15 circulations, +0.25 nm detuning).

In Fig. 4.5, we see the eye-diagrams of input and output signal for the optimized case: +5 ps/nm residual dispersion per loop and +0.25 nm detuning of tunable filters from the input signal's center wavelength. The top pair of eyes is for pulses without artificial degradations, and we can see that the output eye quality is as good as the input. For the purpose of simulating non-ideal ZEROs, we artificially degrade the modulator extinction ratio by varying its bias voltage. In the middle pair of eyes of Fig. 4.5, where we artificially degrade modulator extinction ratio to the level of ~ 7 dB, we observe that regenerated output pulse clearly eliminates noise in ZEROs. To simulate the signal with

amplitude jitter, we interfere the original with co-polarized light from second laser tuned to the same wavelength (in-band cross-talk). For input pulse with 25% amplitude jitter (bottom row in Fig. 4.5), the regenerated pulse has much cleaner amplitude (larger eye-opening).

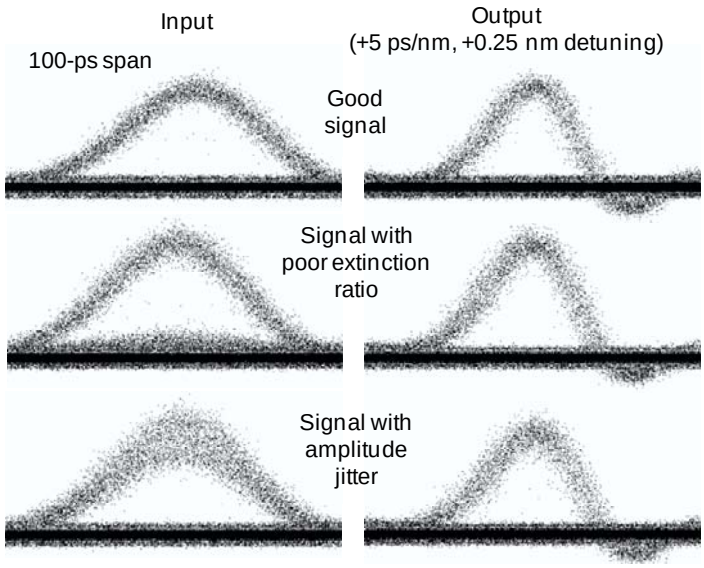

Fig. 4.5. Eyes for signal input (after 0 circulations, no filter detuning) and output (after 15 circulations).

To quantify the signal improvement by the regenerator, we compare curves of bit-error-rate (BER) versus power entering the receiver's optical pre-amplifier. While the regenerator cannot improve the BER detectable by an ideal receiver, it can make the signal more robust with respect to the subsequently added noise. In a noisy receiver, the BER improves with increasing optical power, and the regeneration makes the same BERs achievable at lower optical powers. The resulting horizontal shift of BER vs. power curves is called eye-opening improvement. The BER vs. received power plot of regenerated signal is measured after 15 loop circulations and for +0.25 nm filter

detuning. The eye-opening improvement is demonstrated by the shift of BER vs. received power curves toward lower powers. In Fig. 4.6 we observe that the regenerated signal is more robust to detector noise compared to the input signal. We also see that for signal with large amplitude jitter, the eye-opening is improved by 3 dB and for signal with artificially degraded modulator extinction ratio, the eye-opening is improved by 2.5 dB.

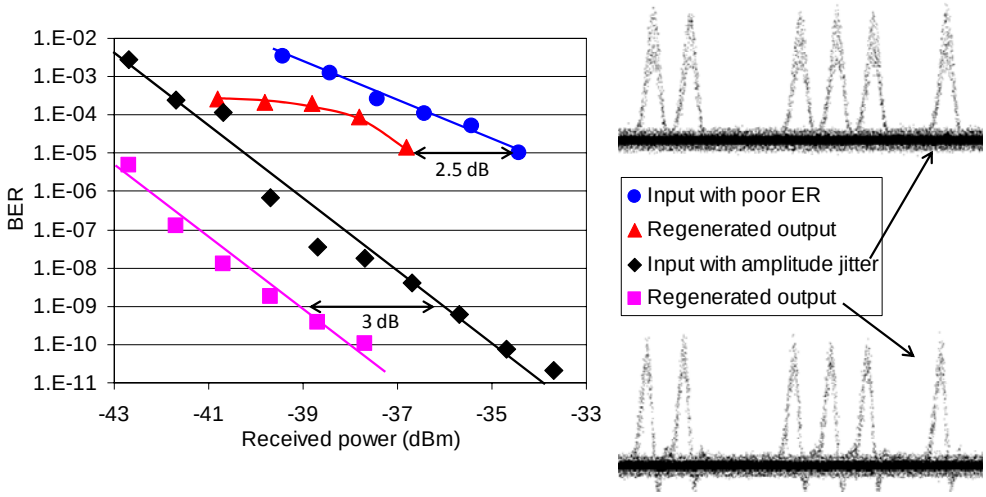

Fig. 4.6. Left: BER vs. received power showing eye-improvement of 3 dB for input pulse with large amplitude-jitter and 2.5 dB for input pulse with poor-ER. Right: Bit patterns for the signal degraded by amplitude jitter before (top) and after (bottom) regeneration.

Thus, the experimental results demonstrate single-channel 2R regeneration in our dispersion-managed scheme, thereby proving that for single-channel, our dispersion-management scheme does not adversely affect the regeneration.

4.2 Multi-channel 2R Regenerator

Our proposed multi-channel 2R regenerator comprises multiple identical HNLF-PGDD sections. For the experimental demonstration of multi-channel 2R regeneration, we use

one HNLF-PGDD section in a recirulcating loop and let the signal circulate through it multiple times. For this task we have designed our loop to work with just a few hundred meters of fiber. Most of the setup is similar to the one used in single-channel experiment (Fig. 4.1), except that in the loop we use 1.25 km of DCF with nonlinear constant $\gamma \sim 5\ W^{-1}km^{-1}$ and dispersion D= −120 ps/nm/km as a nonlinear medium and PGDD as a dispersive medium. The role of PGDD is to compensate the dispersion of the HNLF within each channel, and at the same time, to ensure high accumulated dispersion between the channels, to reduce inter-channel interactions. The PGDD used in our multi-channel experiments is Teraxion's ClearSpectrum™-TDC. The ClearSpectrum™-TDC operation is based on a chirped FBG used in reflection and requires a 4-port optical circulator to collect the dispersion compensated signal and separate it from the input signal (Fig. 4.7).

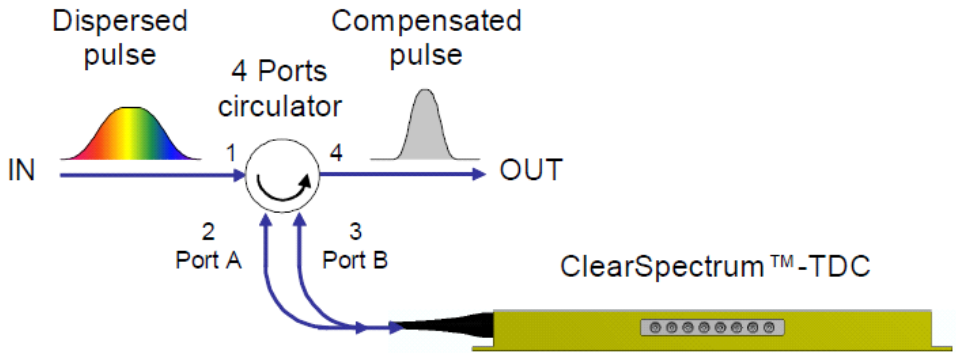

Fig. 4.7. Schematic of Teraxion's ClearSpectrum™-TDC (Model#: TDC27-1527.216-200(-0250/+0250)A01).

The operation of the tunable dispersion compensator (TDC) is based on the thermal control of the FBGs. The ClearSpectrum™-TDC requires two TEC controllers

and a heating element controller to be fully operational. The temperature controllers are manually adjusted to achieve the desired dispersion level. The two gratings of opposite chirps are connected to a 4-port circulator (Port A and Port B) and their overall dispersion is the sum of the dispersion of the individual FBGs (Section 3.2.1). Teraxion, FBG-based TDC is a 27-channel device with 200 GHz channel spacing, covering ITU frequencies from 191.1 THz (1568.8 nm) to 196.3 THz (1527.2 nm). The device has a-1-dB operating bandwidth of 100 GHz and a tuning range from -250 to +250 ps/nm.

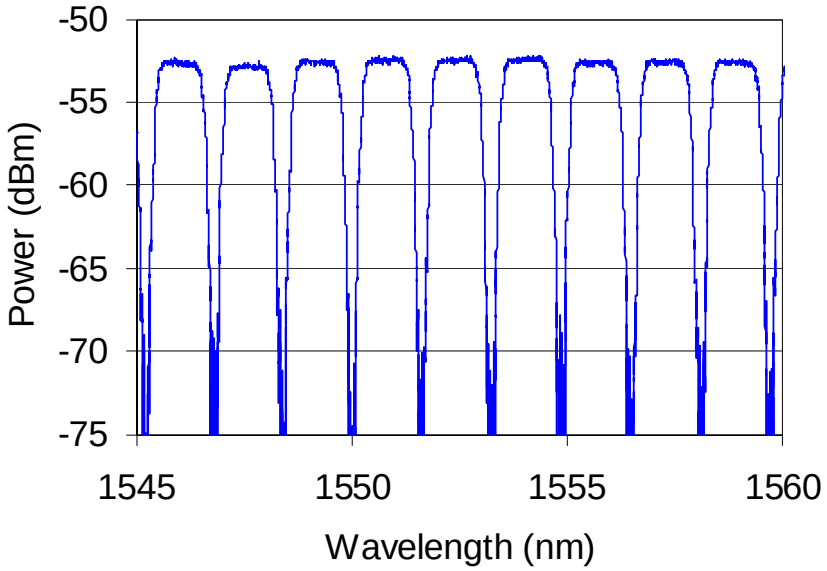

Fig. 4.8. Reflection spectra of Teraxion's ClearSpectrum^{TM}-TDC.

Figure 4.8 illustrates the spectrum of the insertion loss of Teraxion TDC. An ideal dispersion compensating filter adjusts the phase of a signal without introducing any amplitude distortion. However, FBG-based dispersion compensating filters have a frequency- dependent amplitude response due to which different frequency components of a pulse acquire different amplitudes. This amplitude response results in filtering

characteristic of PGDD and destroys the capabilities of our multi-channel regenerator when it is operated in a regime reported in [1]. In [36], a more practical and robust regime is reported that uses a stronger dispersion map compared to the regime in [1], with large and anomalous average dispersion. In this new regime, regenerator requires fewer PGDDs (5 or 6) compared to 16 as reported in [1] and also in this regime, the regenerator's performance is robust not only with respect to the filtering characteristic of PGDD, but also with respect to considerable variations of regenerator parameters (e.g. residual dispersion per loop and filter detuning). Our experimental demonstration of multi-channel 2R regeneration is carried out in this regime with ~ +20 ps/nm residual dispersion per loop. The 1.25-km DCF length in the loop is chosen in accordance with [36]. The bandpass filtering functionality inherent to PGDD also helps in suppressing accumulation of ASE noise between the channels, hence we do not require 1-nm-wide OBPF in the loop.

4.2.1 2-channel Regeneration Experiment

Figure. 4.9 shows a block diagram of 2-channel regeneration experimental setup. The transmitter contains two DFB lasers, one tunable laser source, a 4x1 coupler used as multiplexer, polarization controller (PC), and modulator. The two DFB lasers separated by 200 GHz are combined by a 4x1 coupler. The signals are modulated (50% RZ) with a 10 Gb/s 2^{31}-1 PRBS using a dual-stage MZM. The channels are co-polarized and their patterns are de-correlated by 0.5-km-long DCF. In order to compensate for the losses of modulator, coupler, PC, and DCF, an EDFA is used. After amplification, the signal is injected into the loop by AOS 1. The loop contains 1.25 km of DCF, a high

power EDFA, 5 km of NZDSF, PGDD, and a 4.4-nm-wide OBPF. In order to compensate for the dispersion of DCF and to have about +20 ps/nm residual dispersion per loop, the dispersion at the PGDD was set to +150 ps/nm. The high-power EDFA in the loop amplifies the two channels simultaneously and the amplified signal enters DCF with average power of about 120 mW (average power per channel ~ 60 mW). The VOAs in the loop are used to control the variations in the input signal power of high-power EDFA so that there is no gain tilt at the EDFA output. The signal coming from the loop is filtered by two 0.2-nm-wide OBPFs with cumulative FWHM=20 GHZ and detected by a pre-amplified receiver. In multi-channel experiments, the OBPF performs off-center filtering as well as functions as a demultiplexer and selects channel of interest at the receiver.

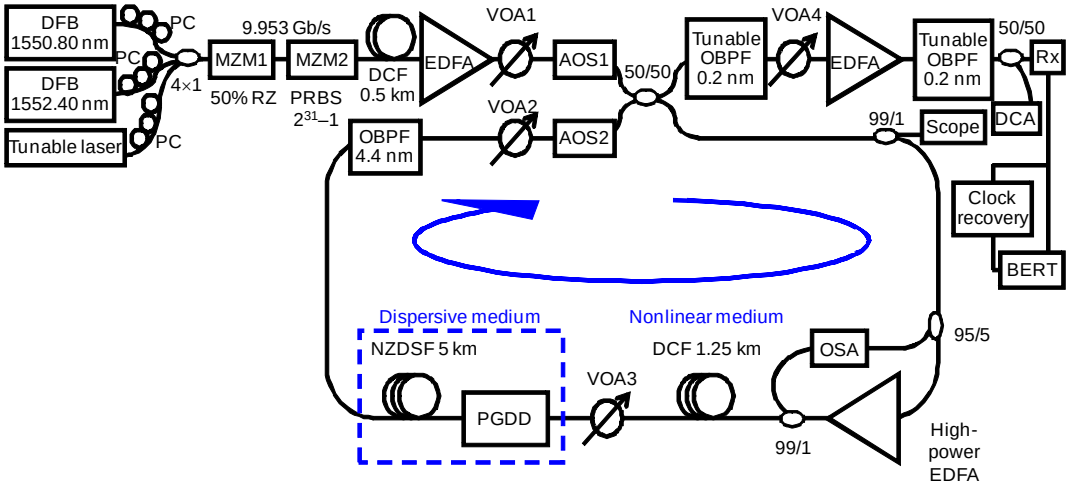

Fig. 4.9. Experimental setup for 2-channel regeneration.

The total length of fiber in the loop (DCF + NZDSF) L_{total} is about 6.25km, and one circulation time is 31.25 μs. As AOS 1 should be left in the ON state for at least one

complete circulation time, the loading-state time was set to 70 μs. The multichannel 2R regeneration experiment needs 7.5 km of DCF. With 1.25 km of DCF in the loop and to attain the total DCF length of 7.5 km, the signal needs to circulate 6 times in the loop. This results in a repetition rate of 3884 Hz, which is set in the trigger menu of SRS 1.

The setup of the triggering equipment is the same as that used in single-channel experiment (Fig. 4.2). All the timing settings of SRS 1 and SRS 2 (Table 4.1) remain unchanged except the trigger rate. The trigger rate is higher as the loop length in 2-channel setup is shorter compared to single-channel experiment.

4.2.2 2-channel Regeneration Results

Figure 4.10 shows the combined 2-channel spectra, measured at OSA with 0.2 nm resolution bandwidth, at the input (circulation #0) and output (circulation #6) of the regenerator.

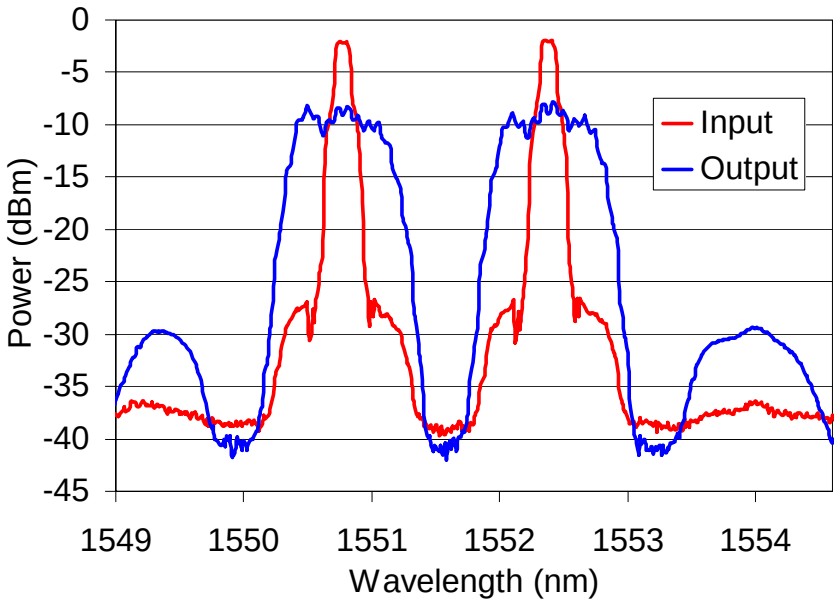

Fig. 4.10. Signal spectra of 2 channels at the input (circulation #0) and output (circulation #6) of regenerator.

As seen in Fig. 4.10, after 6 circulations through the loop both channels undergo equal amount of SPM-induced spectral broadening. In order for both channels to have the same amount of spectral broadening they need to have equal nonlinear phase shifts, and this is achieved by using optimum pre-emphasis technique. The optimim pre-emphasis technique is explained in detail in Section 4.2.5.

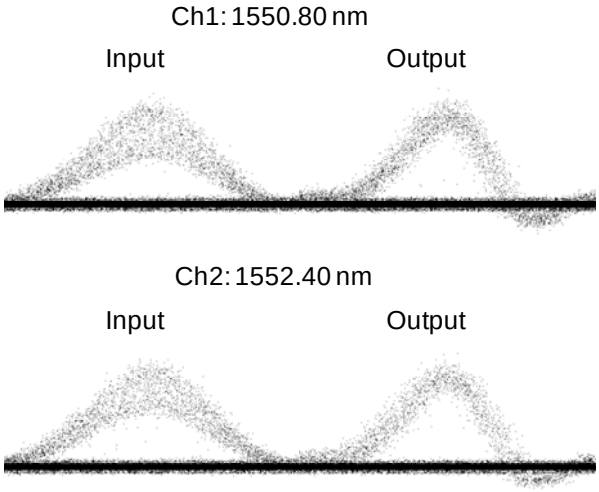

Fig. 4.11. Eyes for signal input (after 0 circulations, no filter detuning) and output (after 6 circulations, +0.17 nm detuning).

For the purpose of simulating the signal's amplitude jitter (±25%), we generate crosstalk by adding a small amount of light from a co-polarized tunable laser source (TLS) adjusted to the same wavelength. Figure 4.11 shows the eye diagrams of both input and the output signals for channel #1 (1550.80 nm) and channel #2 (1552.40 nm), for the optimum value of +0.17 nm detuning of the tunable filters from the input signal's center wavelength. For both channels, the regenerator cleans the fluctuations in the amplitude of the input pulse.

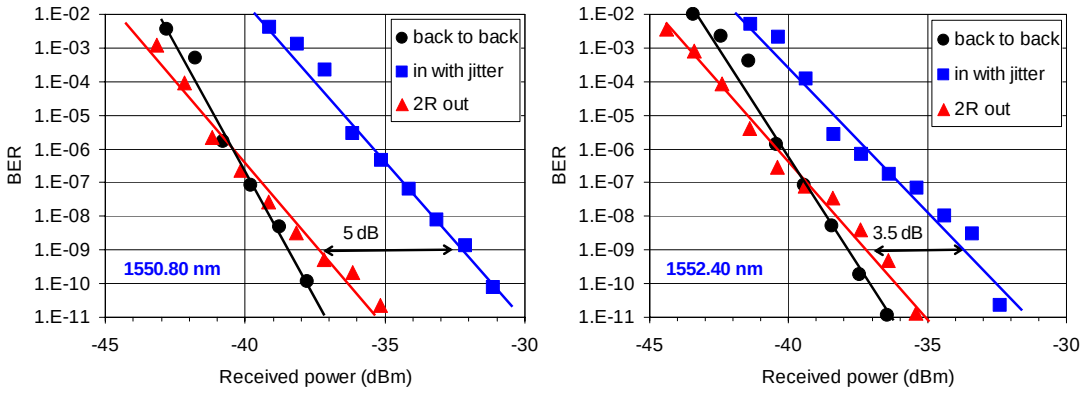

(a) (b)

Fig. 4.12. BER vs. received power measured for an input pulse with large amplitude-jitter, showing an eye-improvement of: (a) 5 dB for channel#1 at 1550.80 nm and (b) 3.5 dB for channel#2 at 1552.40 nm

The 2R regeneration effects are quantified by measurement of eye-opening improvement. Figure 4.12 shows the eye-opening improvements for 2 channels after their simultaneous 2R regeneration, measured by comparing curves of bit-error rate (BER) vs. received power. We observe that for signal with large amplitude jitter, the eye-opening improvements for channel #1 (1550.80 nm) and channel #2 (1552.40 nm) are about 5, and 3.5 dB, respectively. The eye-opening improvement achieved for 1550.80-nm-channel is: 5 dB when operated alone and 5 dB when operated in the presence of second channel at 1552.40 nm. This shows that there are no degradations due to addition of second channel.

4.2.3 8-channel Regeneration Experiment

Figure 4.13 shows the schematic of 8-channel experiment using a recirculating loop setup. We generate 8x10 Gb/s channels spaced 200 GHz apart (from 1545.99 nm to 1557.27 nm) by interleaving two co-polarized sets (4 odd channels multiplexed by AWG1 and 4 even channels multiplexed by AWG2) of 400-GHz-spaced WDM

channels. These two sets of WDM channels are modulated (50% RZ) by two independent pattern generators (2^{31}-1 PRBS) driven by slightly different clock frequencies. To ensure that we study a realistic worst-case scenario of co-polarized un-correlated WDM channel, all the channels originating from same pattern generator are co-polarized and their PRBS patterns are decorrelated by 0.5-km-long DCF. The ±25% amplitude jitter is simulated by adding a small amount of light from a co-polarized laser source tuned to the signal wavelength. At the receiver, signals are selected, one at a time, by two 0.2-nm-wide OBPFs. The high-power EDFA in the loop amplifies all the 8 channels simultaneously and the amplified signal enters DCF with average power of about 480 mW (average power per channel ~ 60 mW). The VOAs in the loop are used to control the variations in the input signal power of high-power EDFA so that there is no gain tilt at the EDFA output.

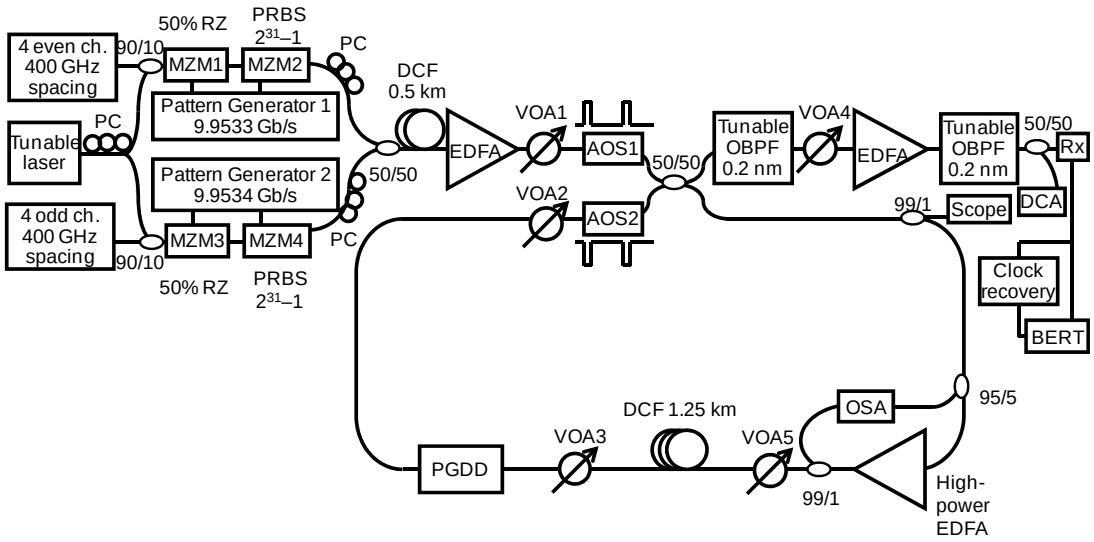

Fig. 4.13. Recirculating loop setup for 8-channel 2R regeneration.

The total length of fiber in the loop is about 1.25 km. Using L_{total}= 1.25 km, we obtain circulation time of 6.25 μs. The loading-state time was set to 50 μs. With 1.25 km of DCF in the loop, the number of circulations is set to 6. This results in the total 5-loop time of 37.5 μs and a repetition rate of 11429 Hz. Since this frequency is higher than maximum 5 kHz frequency of the OSA external trigger, we used "LPF" setting on the OSA. In order to eliminate the potential nonlinearities in the NZDSF, all dispersion compensation (~ +170 ps/nm) is carried out by the PGDD.

The setup of the triggering equipment is same as that used in single-channel experiment (Fig. 4.2). The timing settings of SRS 1 and SRS 2 (Table 4.1) are slightly different as the round trip time is very short compared to single- and 2-channel experiments. The width of the gating pulse is reduced to 3 μs, as it should be smaller than T_{circ} which is 6.25 μs. The measurement window selects the regenerated signal at 6th circulation for characterization at OSA, BER tester and DCA.

4.2.4 8-channel Regeneration Results

Figure. 4.14 (a) shows the signal spectra for 8 channels at the input and output of regenerator. A pre-emphasis technique is used to ensure all 8 channels have similar nonlinear phase shifts. As seen in Fig. 4.13 (a), all the channels undergo equal amount of SPM-based spectral broadening. Figure 4.14 (b) shows the signal spectra for channel #4 (1550.80 nm) after 6 circulations in the loop. In Fig. 4.13 (b), we can see that the spectrum broadens and flattens at the top which is similar to the conventional 2R regenerator with constant dispersion.

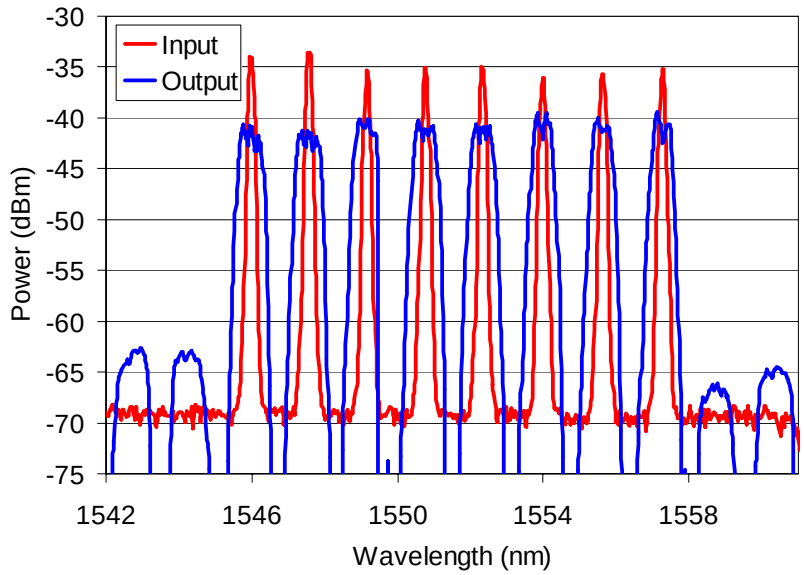

(a)

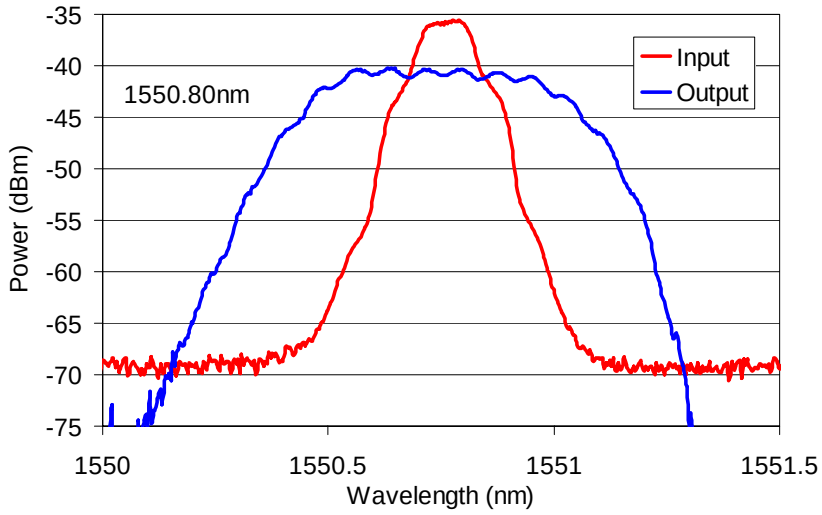

(b)

Fig. 4.14. Signal spectra of (a) all 8 channels and (b) channel #4 (1550.80 nm), at the input and output of regenerator.

Figure 4.15 shows eye-diagrams of the degraded input signal and regenerated output signal for channel #4 (1550.80nm) after 6 circulations in the loop and for

optimum value of +0.15 nm detuning of tunable filters from the input signal's center wavelength. The regenerator significantly improves the optical eye by cleaning the amplitude jitter of the input pulses.

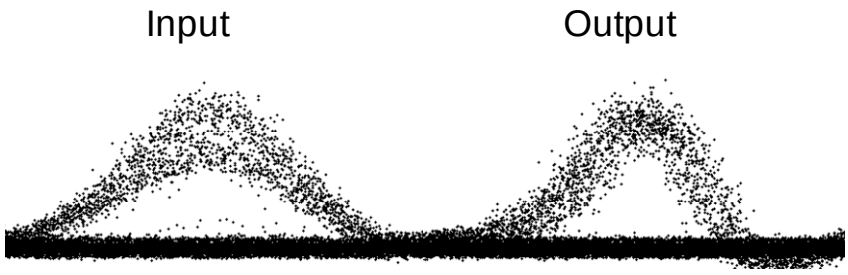

Fig. 4.15. Eyes diagrams for channel #4 (1550.80 nm), at the input (circulation #0) and output (circulation #6) of the regenerator.

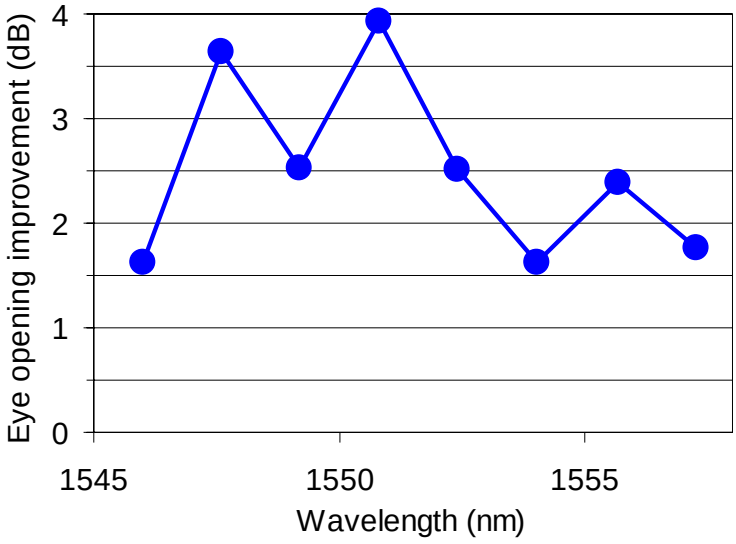

Fig. 4.16. Eye-opening improvements for each of the 8 channels, measured at BER of 10^{-9} and for the optimum value of +0.15 nm filter detuning.

The 2R regeneration effects for all 8 channels are quantified by measurement of eye-opening improvement. The eye-opening improvement for all the eight channels after their simultaneous 2R regeneration is measured by comparing curves of BER vs.

received power. In Fig. 4.16 we can see that for all 8 channels the eye-opening improvement at BER of 10^{-9} and +0.15 nm filter detuning is greater than 1.6 dB.

4.2.5 12-channel Regeneration Experiment

Figure. 4.17 shows the schematic of 12-channel regeneration experiment. Most of the setup is similar to the one used in 8-channel experiment (Fig. 4.13), except that a 12-channel WDM transmitter is used instead of 8-channel. All 12 channels are evenly spaced in frequency and the channel spacing is 200 GHz. Due to malfunctioning of the PGDD, its passband has shifted by ~ 0.4 nm toward shorter wavelengths. We had to adjust our channel plan accordingly, making the DFBs centered from 1550.80 nm to 1550.40 nm. The odd and even set of channels are combined separately by two different AWGs and modulated with different data patterns (10 Gb/s, 2^{31}-1 PRBS), to ensure that neighboring channels are uncorrelated at the receiver. In addition, all channels are co-polarized and their patterns are decorrelated by 0.5-km-long DCF. The outputs of the modulators are combined onto a single fiber, amplified and injected into the loop. The input signal is artificially degraded by adding a small amount of light from a co-polarized laser source tuned to the signal wavelength. After five circulations in the loop, the particular channel of interest is selected by two 0.2-nm-wide OBPFs.

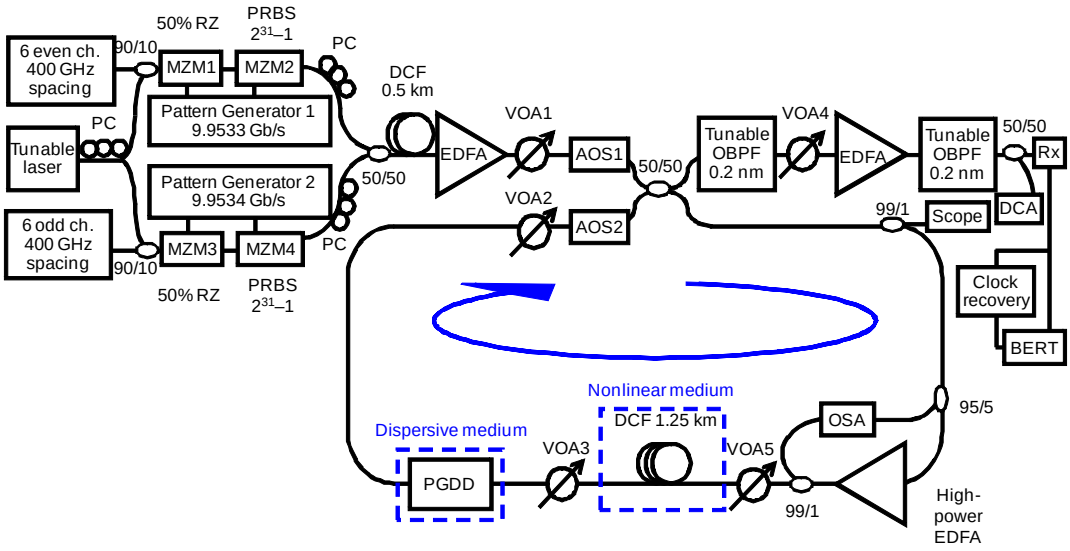

Fig. 4.17. Experimental setup for 12-channel regeneration.

The high-power EDFA in the loop amplifies all the 12 channels simultaneously and the amplified signal enters DCF with average power of about 720 mW (average power per channel ~ 60 mW). In our experiments, we do not employ gain flattening filter, instead we use pre-emphasis technique to avoid ripple accumulation with increasing number of loop circulations. For a relatively small gain ripple, the optimum pre-emphasis technique enforces a straight line spectrum near the middle of the link [37]. This scheme results in uniform OSNR and Q performance among all the channels. In the presence of distortion-like nonlinearity such as SPM, this technique ensures all WDM channels have equal nonlinear phase shifts [37].

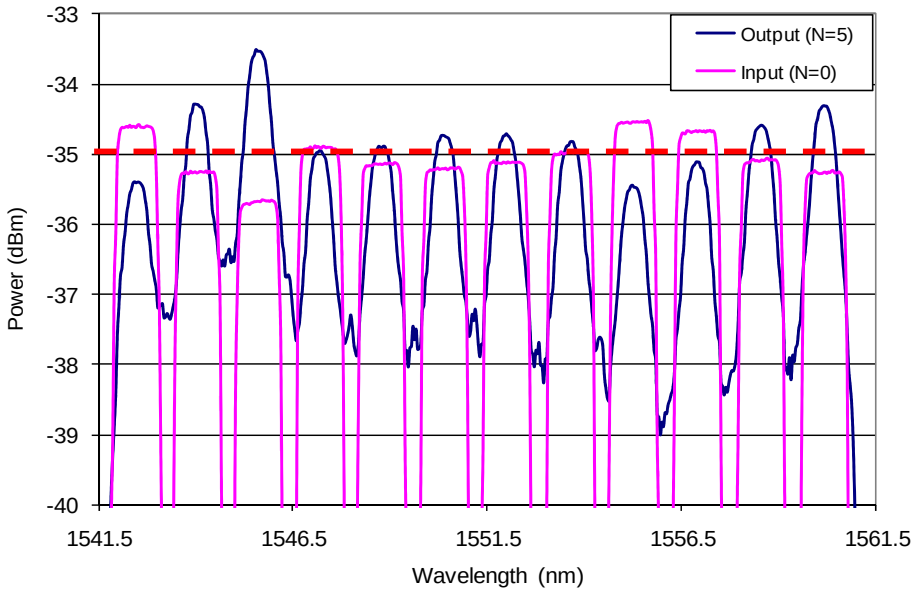

Fig. 4.18. Pre-emphasis technique producing a straight-line spectrum halfway between circulation #0 and circulation #5: average power of 12 channels at circulation #0 and circulation #5 measured at OSA (5% tap in the loop) with 2 nm RBW. Dashed line is the line of approximate inversion symmetry.

Figure 4.18 shows the powers of all 12 channels: at the input of the DCF in the first circulation and at the output of the DCF in the 5th circulation through the loop. The EDFA gain ripple is observed at OSA at 5% tap in the loop. We pre-emphasize the spectrum at the input of first circulation such that the spectral ripple has approximately same magnitudes and opposite signs before first circulation and after 5 circulations. As a result, the spectrum halfway between circulation #0 and circulation #5 is flat. As seen in Fig. 4.19, the pre-emphasis technique enforces the spectral ripples at circulation #0 and circulation #5 to be inverted versions of each other.

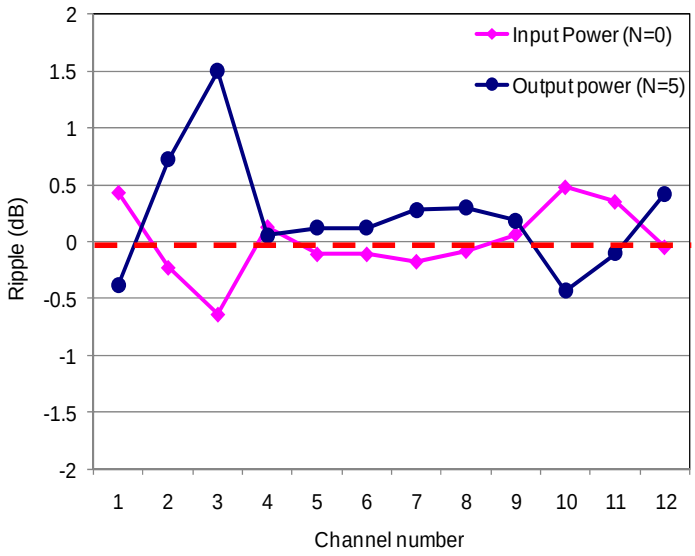

Fig. 4.19. Pre-emphasis technique producing a straight-line spectrum halfway between circulcation #0 and circulation #5: gain ripple at circulation #0 and circulation #5 (2 nm RBW of OSA).

The total length of fiber in the loop is about 1.25 km which results in circulation time of 6.25 μs. The loading-state time is set to 50 μs. Here, the best performance is achieved after 5 circulations in the loop (i.e. after total 6.25 km of DCF). This results in a repetition rate of 12308Hz. The trigger set up and timing settings at SRS 1and SRS 2 are same as in 8-channel experiment. The measurement window selects the regenerated signal at after 5 circulations for characterization at OSA, BER tester and DCA.

4.2.6 12-channel Regeneration Results

Figure. 4.20 (a) shows the signal spectra for 12 channels at the input and output of regenerator. As mentioned in previous section, the pre-emphasis technique ensures all twelve channels have similar nonlinear phase shifts. As a result, all the channels undergo equal amount of SPM-based spectral broadening. Figure 4.20 (b) shows signal spectra of channel #6 (1550.40 nm) after 0 through 7 circulations. As the signal

propagates through increasing number of circulations, its spectrum broadens symmetrically. However, for circulations greater than 5 broadening is limited by the PGDD passband.

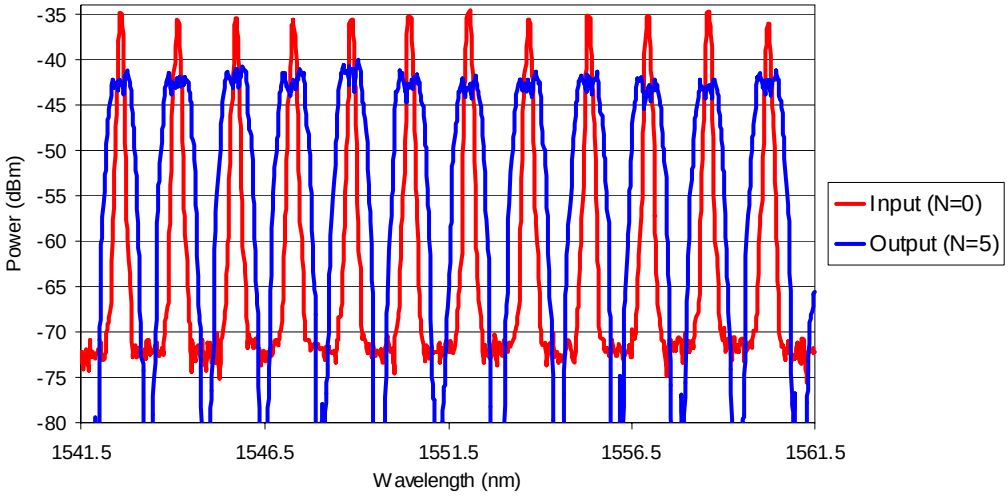

(a)

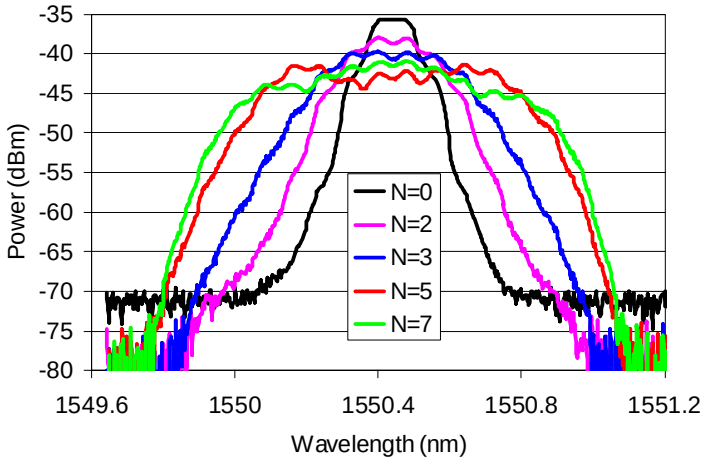

(b)

Fig. 4.20. Signal spectra of (a) all 12 channels and (b) channel #6 (1550.40 nm), at the input and output of regenerator (0.2 nm RBW at OSA).

Figure 4.21 shows the eye-diagrams of degraded input signal (±25% amplitude jitter) and regenerated output signal for all 12 channels after 5 circulations in the loop and for optimum value of +0.15 nm detuning of tunable filters from the input signal's center wavelength. For all 12 channels we can see that the regenerated output pulse much has a much cleaner amplitude compared to the input pulse.

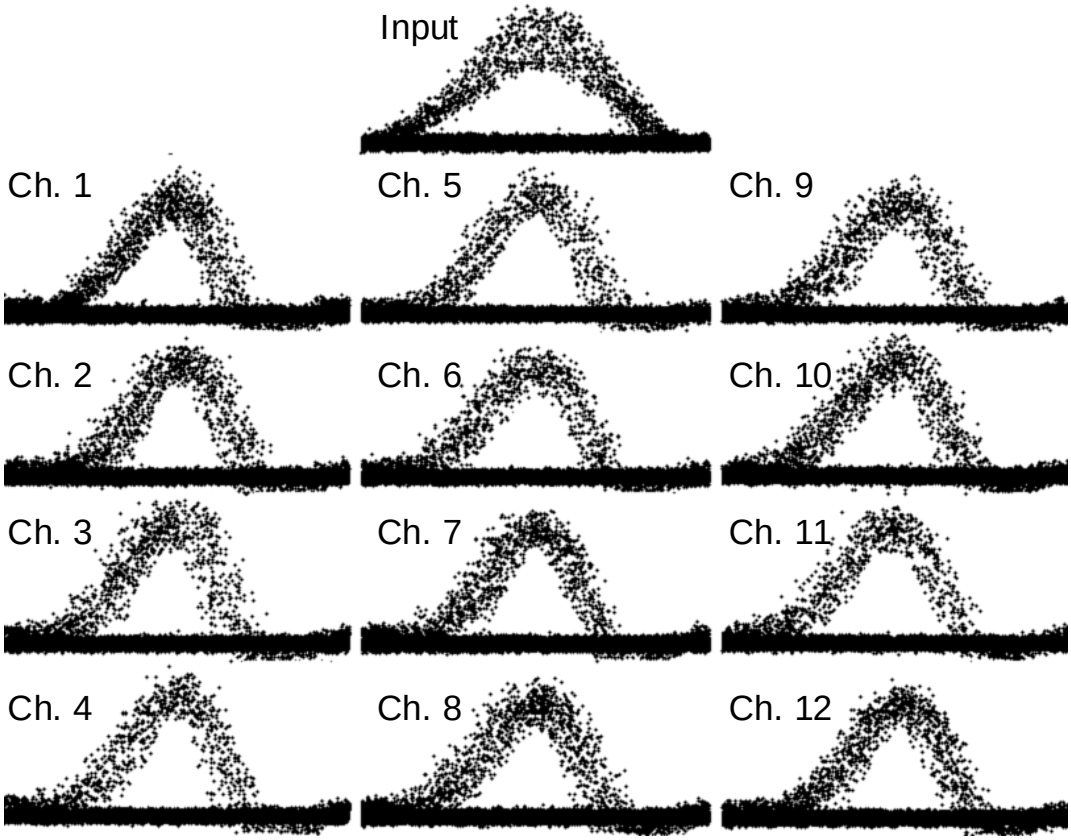

Fig. 4.21. Eyes diagrams for 12 channels at the input (circulation #0) and output (circulation #5) of the regenerator.

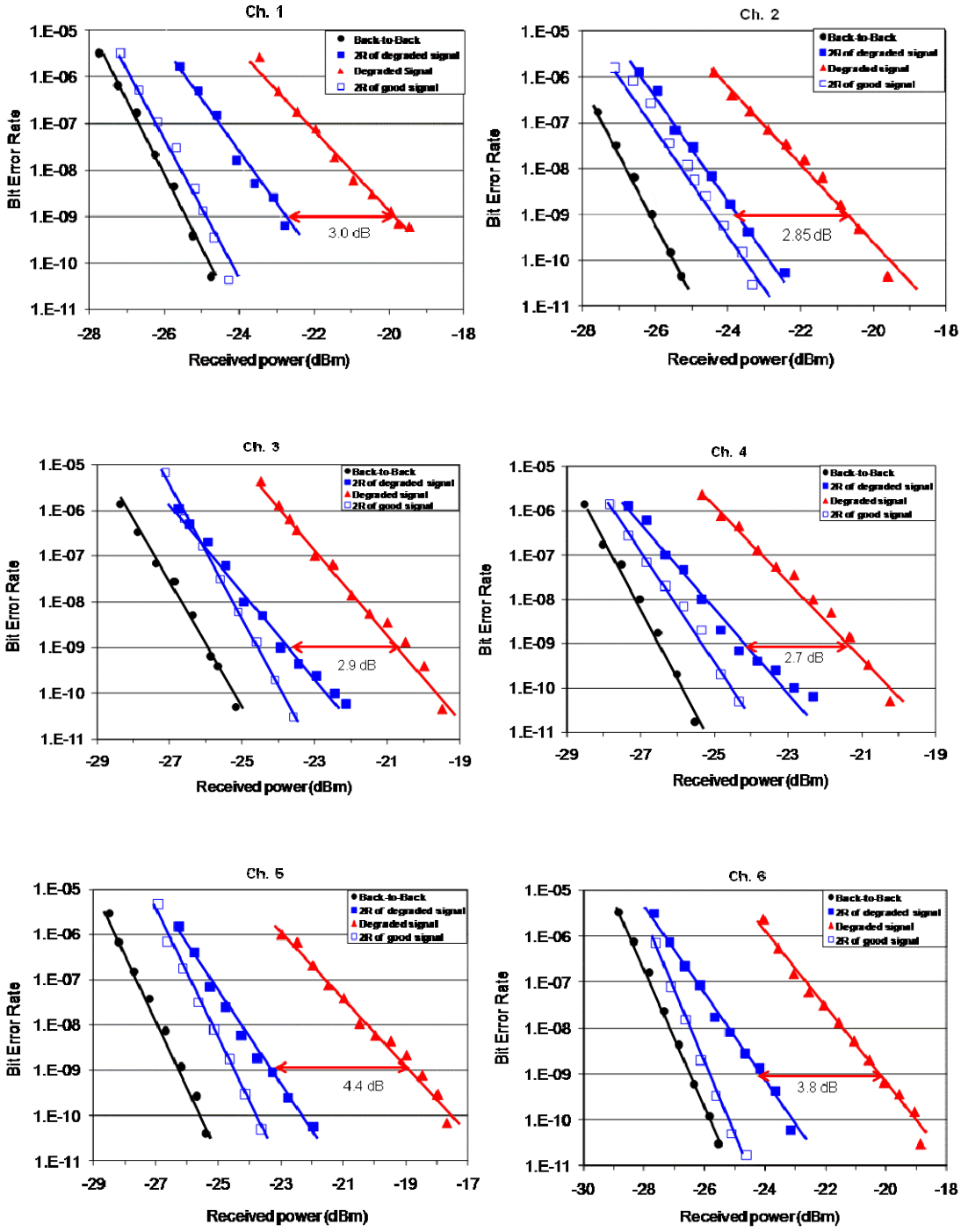

Fig. 4.22. BER vs. received power measured for channels 1 – 6: artificially degraded input signal (red solid triangles), regenerated output of degraded input signal (blue solid squares), regenerated output of good input signal (blue open squares), and good input signal in Back-to-Back arrangement (black solid circles).

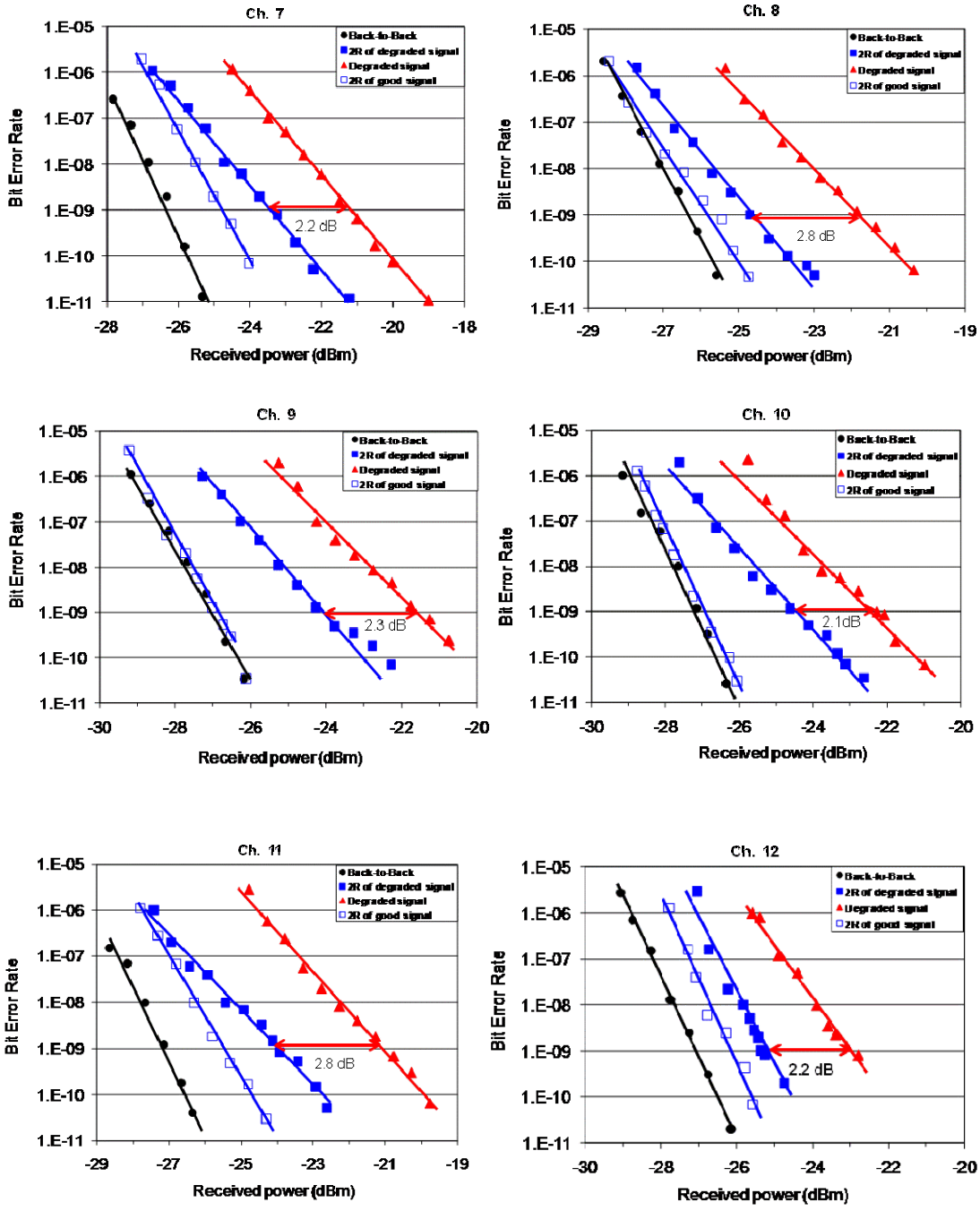

Fig. 4.23. BER vs. received power measured for channels 7 - 12: artificially degraded input signal (red solid triangles), regenerated output of degraded input signal (blue solid squares), regenerated output of good input signal (blue open squares), and good input signal in Back-to-Back arrangement (black solid circles).

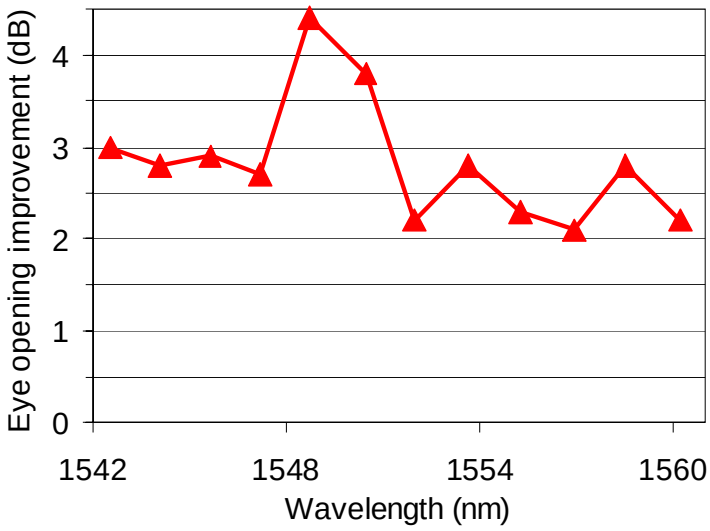

Fig. 4.24. Eye-opening improvements for each of the 12 channels, measured for the optimum value of +0.15 nm filter detuning.

The eye-opening improvements for all twelve channels after their simultaneous 2R regeneration is measured by comparing curves of the BER vs. received power. Figures 4.22 and 4.23 show the BER vs. received power plots measured for all 12 channels. For back-to-back measurements, the output of modulator is directly connected to the receiver's 0.2-nm OBPF, and the BER curve is measured to estimate the baseline performance of the measurement system. The BER vs. received power plot of regenerated output signal is measured after 5 loop circulations and for +0.15 nm detuning of tunable filters from the input signal's center wavelength. When the regenerator acts on a good signal, some degradation is observed, because the effects of loop loss and noise figure of the high-power EDFA are noticeable when added to the clean signal. However, when we use the input signal with ±25% amplitude jitter, clear eye-opening improvements are observed for all 12 channels. In Fig. 4.24, we see that

for all twelve channels the eye-opening improvement at BER=10^{-9} and +0.15 nm detuning is greater than 2 dB.

Figure 4.25 illustrates performance of regenerator with respect to filter detuning. Eye-opening improvement vs. filter detuning is measured for channel #6 at circulation #5. The filter detuning is varied from −0.25 nm to +0.25 nm and in Fig. 4.25 we can see that regeneration is insensitive to moderate change in filter detuning. Some asymmetry between the positive and negative detuning performance stems from the fact that the centers of the PGDD passbands and the 12-channel DFB grid do not completely coincide. The optimum regenerator operating point suitable for all 12 channels is after 5 circulations in the loop and with +0.15 nm filter detuning.

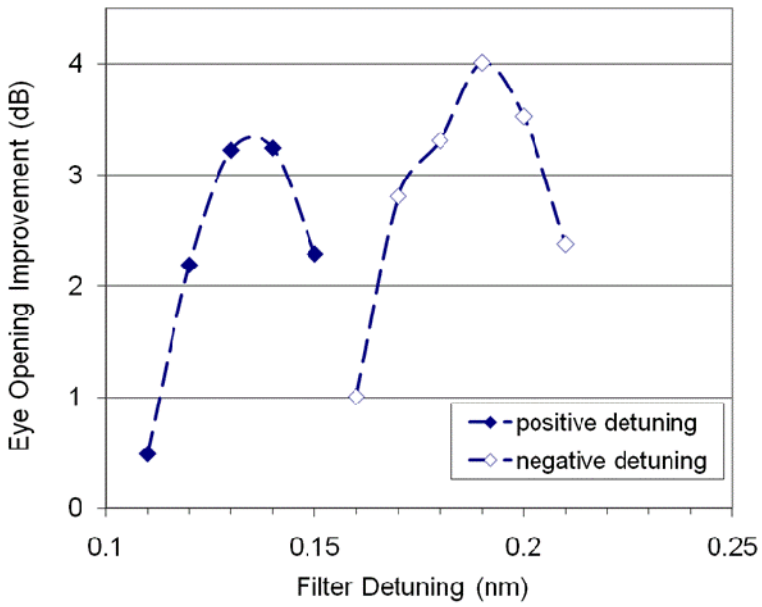

Fig. 4.25. Effect of change in filter detuning on regeneration, measured for channel #6 after 5 loop circulations.

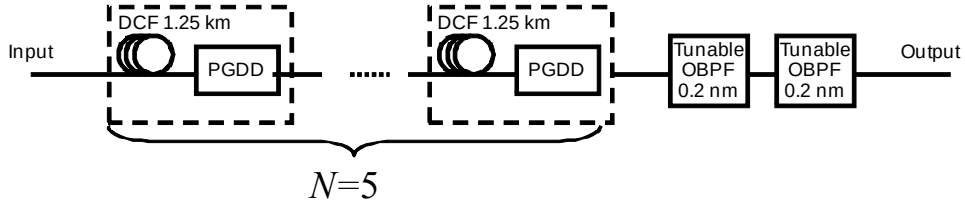

Fig. 4.26. Schematic of multi-channel 2R regenerator for input-output transfer function measurements.

Figure 4.26 shows an effective block diagram of our regenerator. Here, each DCF-PGDD cell represents one circulation through the loop. The input power of regenerator is the average power of signal measured at the input of DCF of first cell. The output power of regenerator is measured at the output of second OBPF after signal completes 5 circulations in the loop. The two OBPF's are detuned by +0.15 nm with respect to the input signal's wavelength. Figure 4.27 shows the output power of filtered signal as a function of its corresponding input power, measured after various numbers of circulations for 3 representative channels, with all 12 channels present in the regenerator. In our regeneration experiments, the optimum value of average power to achieve sufficient spectral broadening in DCF is 60 mW per channel (10 Gb/s, 50% RZ). As seen in Fig.4.27, for all 3 selected channels, when the average power of the input signal is less than 60 mW (i.e. the peak power of input pulses less than 250 mW), the pulses do not induce enough SPM and are rejected by the filter. When the average power is high enough (> 60 mW), a part of the SPM-broadened spectrum passes through the off-centered filters. This results in a nonlinear transfer function that reduces both the noise in ZERO symbols and the fluctuations of ONE symbols. Further, Fig. 4.27 shows input-output transfer function for channel #6 measured for a number of *N*

circulations through the loop.

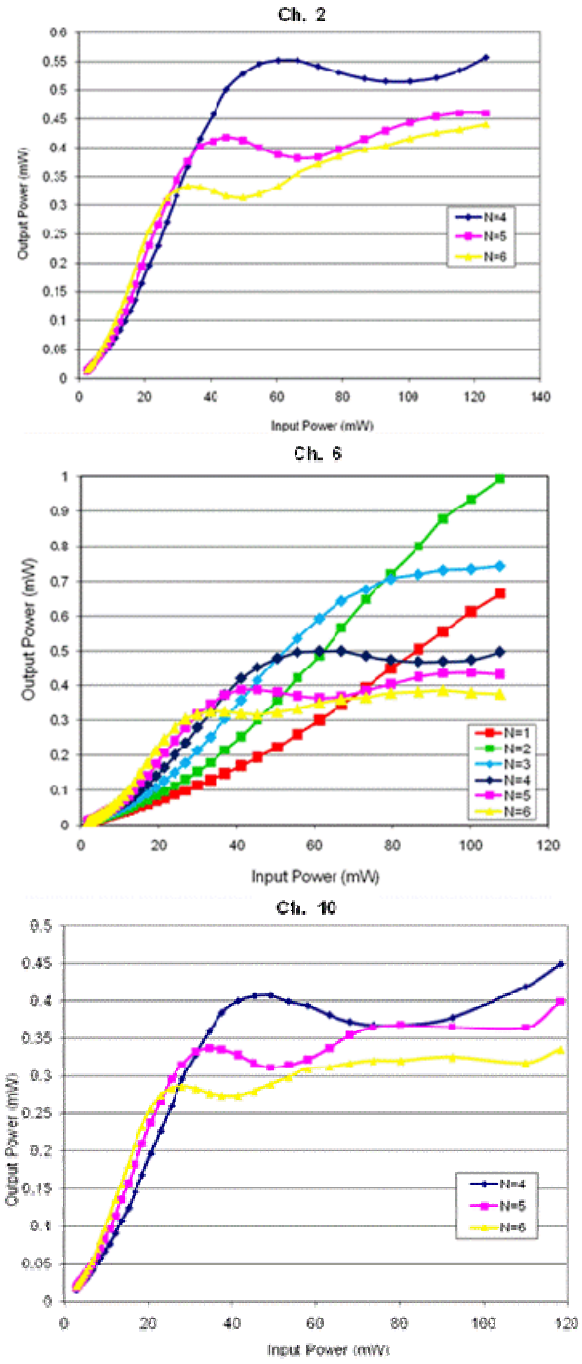

Fig. 4.27. Power transfer curves of 12-channel regenerator after *N* circulations. Output power measured with +0.15 nm filter detuning for 3 representative channels: channel #2 (1544.03 nm), channel #6 (1550.40 nm) and channel #10 (1556.87 nm).

In Fig. 4.27 we can see that for fewer number of circulations through the loop (N = 1, 2, 3), the transfer function is linear as the spectrum is not sufficiently broadened. As the number of circulations increases (N = 4, 5, 6), we observe that for 3 channels the input-output curves have a flat plateau as predicted by the 2R regenerator theory [2].

In order to confirm that our dispersion map makes the inter-channel nonlinear interaction insignificant, we have characterized the performance of multi-channel regenerator at one channel versus the number of neighboring channels, since the main nonlinear crosstalk component in WDM systems comes from the adjacent channels. In 2-channel experiment, the eye-opening improvement of 1550.80-nm-channel is measured for two cases: channel operated alone and, when operated in the presence of second channel at 1552.40 nm. As seen in Fig. 4.28, there are no degradations due to the addition of second channel. The green curve in Fig. 4.28 shows the 1550.80 nm channel performance with the progression of our experiments having total of 4, 6, 8, and 12 channels (1550.41 nm for the latter case). Again, no degradation with increased number of channels is observed. Finally, we measure 1550.4 nm channel performance at fixed total number of 8 channels, but with varying number of neighboring channels. For this task, we vary the number of channels around the channel at 1550.4 nm and measure the eye-opening improvement of this channel for each arrangement (blue curve in Fig. 4.28). We can see that the performance of regenerator does not degrade eye when the number of neighboring channels is increased from 0 to 7. The three curves (pink, green, and blue) in Fig. 4.28 were measured in three separate experiments. The pink curve in Fig. 4.26 shows the eye-opening improvements measured in 2-channel

experiment. The high-power EDFA (fiber amplifier from Optocom Innovation, which later became Keopsys) used in our 2-channel experiment has different optical characteristics compared to the high-power EDFA (IPG Photonics) used in our 8- and 12-channel experiments. Also, the total length of loop (5km of LEAF + 1.25km of DCF) in our 2-channel experiments was different compared to the length of loop (1.25km of DCF) in 8- and 12-channel experiments and, as a result, the loop settings were different. The blue and green curves in Fig. 4.28 were measured using same loop settings (1.25km of DCF in the loop). Also, in both experiments IPG high-power EDFA was used in the loop. However, the experiments were carried out with different output power settings on the IPG high-power EDFA. The actual output power of IPG EDFA, measured with a power meter, is about 2.65 dB more than the output power reading on the IPG screen (i.e. IPG 100 mW reading = 22.65 dBm at Power meter). As a result, a VOA was used after the EDFA (VOA5 in Fig. 4.13 and 4.17) in the loop in order to adjust the power input to the DCF. The blue curve in Fig. 4.28 was measured by setting the output power on the IPG screen to the minimum allowed value of 500 mW (8 channels ON: power per channel = 8x60 mW ~ 500 mW) and by adding attenuation of ~ 2.65 dB at VOA5 (Fig. 4.13 and 4.17). The green curve in Fig. 4.28 was measured by changing the output power of IPG and by varying the attenuation at VOA5 (Fig. 4.13 and 4.17) depending on the total number of channels used in the experiment.

As the curves (pink, green, and blue) in Fig. 4.28 were measured in three separate experiments, using different EFDA and loop settings, no comparison should be made between the curves of different colors.

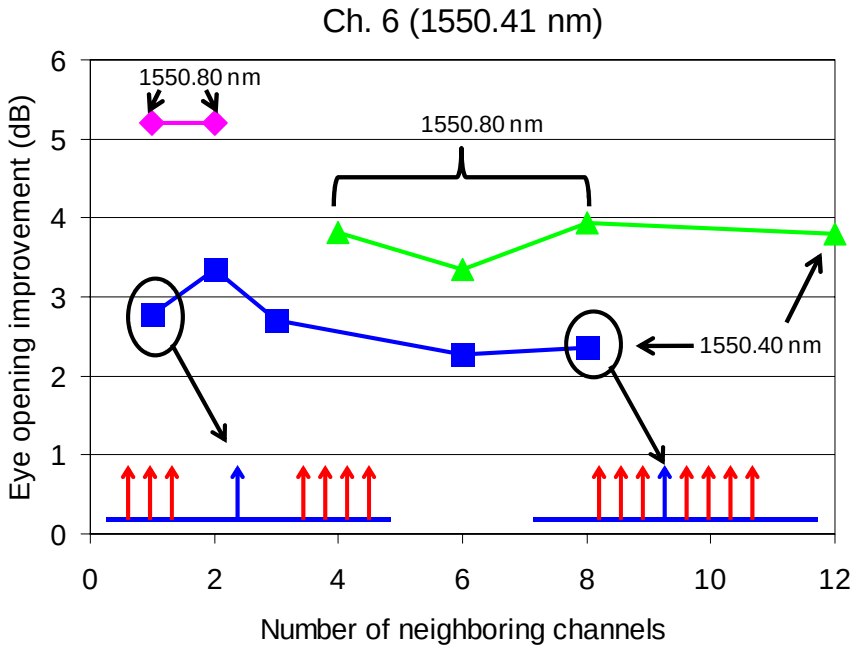

Fig. 4.28. Regenerator performance of our center-channel (1550.41 nm or 1550.80 nm) with respect to the total number of channels. Three curves (pink, green, and blue) were measured in three separate experiments using different EDFA and loop settings.

This confirms that there are no degradations due to inter-channel nonlinearities and proves that our dispersion-managed regenerator performs efficient multi-channel regeneration while suppressing nonlinear inter-channel crosstalk.

CHAPTER 5

FUTURE WORK

As mentioned in the previous chapters, our proposed and demonstrated multi-channel regenerator consists of multiple HNLF-PGDD sections. Multiple PGDDs in our proposed regenerator scheme are not expected to contribute significantly to the passive loss, cost, and physical dimensions of the regenerator, as in the future they can be integrated on low-loss planar lightwave circuits [38,39], with good match between the HNLF and PGDD mode sizes [40]. The future work beyond this thesis is practical realization our multi-channel 2R regenerator, by integrating all PGDDs, using planar lightwave technology, on a single chip. An important task in this work would be to design a multi-channel dispersion compensator which can be practically implemented using a compact low-loss planar waveguide technology. Planar lightwave circuits (PLCs) or Planar Integrated Circuits (PICs) are optical chips that are mostly used in fiber optic communication networks to perform various functions such as wavelength filtering, optical switching, and optical channel power control [41]. In WDM systems, PLCs play a significant role, serving mainly as channel multiplexers and demultiplexers. Recently, in long haul communication systems operated at bit rates of 10 Gb/s or higher, PLCs have been also used as dispersion compensators and optical equalizers. An all-pass optical filter which has the potential for multi-channel dispersion compensation has been demonstrated as a low-loss compact device using ring

resonators in planar waveguides [38, 42]. Optical all-pass filters are very attractive as dispersion compensating filters, as they allow phase correction without introducing any amplitude distortion and also, can correct for any order of dispersion [43]. An ideal lossless all-pass filter has a unity magnitude response, and its phase response can be altered to approximate a desired response [43]. This chapter focuses on designing a multi-channel dispersion compensating all-pass filter, using ring resonators, to compensate the dispersion of HNLF in our 2R regenerator and to have an optimum residual dispersion of about +20 ps/nm per HNLF-PGDD cell.

5.1 Multi-stage Dispersion Compensating All-pass Filter

One of the common implementation of the optical all-pass filter is a ring resonator. A basic single-stage all-pass filter using one ring resonator is shown in Fig. 5.1. As seen in the Fig. 5.1, a single-stage ring all-pass filter is a two port device consisting of a ring resonator, a coupler, and a waveguide. The ring and the waveguide are evanescently coupled and, the amount of light coupled into and out of the ring is determined by the coupling efficiency κ of the coupler. Similarly to a conventional beam splitter, the coupling coefficient κ is directly related to the transmission coefficient r of the coupler (we use the notation "*r*" to show its similarity to the reflection coefficient of a beam splitter) as $\kappa^2 = 1 - r^2 = 1 - R$.

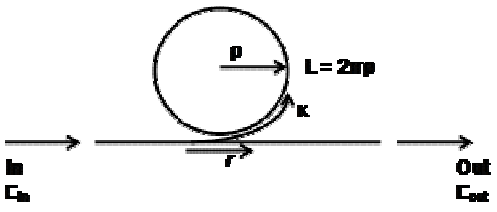

Fig. 5.1. A basic single-stage all-pass filter ring resonator.

The cavity resonates when the length ($L = 2\pi\rho$) of a roundtrip is an integer multiple of the wavelengths in the ring. The free spectral range (FSR) is the frequency spacing between two consecutive resonant peaks. For a ring all-pass filter, the FSR is defined in the frequency domain as the difference $\Delta\nu$ between two consecutive resonance frequencies and is given as follows,

$$FSR = \Delta\nu = \frac{c_g}{L} = \frac{c_g}{2\pi\rho} = \frac{1}{T_{rt}}, \tag{5.1}$$

Here, L is the circumference of a ring, ρ is the radius of the ring, $c_g = c/n_g$ is the group speed of light in the ring material, and T_{rt} is one roundtrip time in the ring cavity. As seen in equation 5.1, the FSR of a cavity is inversely proportional to the roundtrip period, which in turn is determined by the length of the cavity. As FSR is inversely proportional to the radius of the ring, small ring radii are required in order to obtain large FSR values. The input-output transfer function of a ring cavity, which is the ratio of the amplitude of the output wave to the amplitude of the incident wave, is given by,

$$\frac{E_{out}}{E_{in}} = \frac{r + e^{-\frac{\delta}{2}} e^{ikL}}{1 + re^{-\frac{\delta}{2}} e^{ikL}} \tag{5.2}$$

Here, r is the reflection coefficient of the cavity, k is the propagation constant, and L is the length of the cavity. The parameter $\delta = \alpha L$, where α is the loss per unit length inside the ring, represents the circulation loss factor in the ring. For a lossless cavity, $\delta = 0$ and the resonator transfer function can be expressed as,

$$\frac{E_{out}}{E_{in}} = \frac{r + e^{ikL}}{1 + re^{ikL}} = \frac{r + e^{i\frac{\omega}{c_{ph}}L}}{1 + re^{i\frac{\omega}{c_{ph}}L}} . \tag{5.3}$$

In equation 5.3, the propagation constant k is expressed as $k = \omega/c_{\text{ph}}$, where $c_{\text{ph}} = c/n$ is the phase velocity of light in the ring. Using the ring resonator input-output transfer function, we can write the magnitude as,

$$\left|\frac{E_{out}}{E_{in}}\right|^2 = \left|\frac{r + e^{i\frac{\omega}{c_{ph}}L}}{1 + re^{i\frac{\omega}{c_{ph}}L}}\right|^2 = \left|e^{i\frac{\omega}{c_{ph}}L}\right|^2 \left|\frac{1 + re^{-i\frac{\omega}{c_{ph}}L}}{1 + re^{i\frac{\omega}{c_{ph}}L}}\right|^2 = 1 . \tag{5.4}$$

The phase response of a single-stage lossless all-pass filter is given by,

$$\varphi(\omega) = \frac{\omega L}{c_{ph}} - 2\tan^{-1}\left[\frac{r\sin\left(\frac{\omega L}{c_{ph}}\right)}{1 + r\cos\left(\frac{\omega L}{c_{ph}}\right)}\right]$$

Two parameters that control the group delay response of a single-stage all-pass filter (Fig. 5.1) are the roundtrip phase, $\omega L/c_{\text{ph}}$, and the coupling coefficient κ [43]. The group delay of an all-pass filter is defined as the derivative of the phase with respect to the angular frequency as follows,

$$\tau = \frac{d\varphi(\omega)}{d\omega} \tag{5.5}$$

The group delay of a single-stage lossless all-pass filter is given by,

$$\tau = \frac{d}{d\omega}\left[\frac{\omega L}{c_{ph}} - 2\tan^{-1}\left(\frac{r\sin\left(\frac{\omega L}{c_{ph}}\right)}{1 + r\cos\left(\frac{\omega L}{c_{ph}}\right)}\right)\right] \tag{5.6}$$

$$\tau = \frac{\frac{L}{c_g}(1-R)}{1 + R + 2\sqrt{R}\cos\left(\frac{\omega L}{c_{ph}}\right)} = \frac{T_{rt}(1-R)}{1 + R + 2\sqrt{R}\cos(2\pi\nu T_{rt})} \tag{5.7}$$

Here, $\omega = 2\pi\nu$ is the angular frequency, ν is the optical frequency, and $R = r^2$ is the "reflectance" of the coupler. The group delay can be further simplified as,

$$\tau = \frac{T_{rt}}{\frac{1-\sqrt{R}}{1+\sqrt{R}} + \frac{4\sqrt{R}}{1-R}\cos^2(\pi\nu T_{rt})} \tag{5.8}$$

An all-pass filter has a periodic group delay response and the period is equal to the FSR. The dispersion is the derivative of the group delay with respect to the vacuum wavelength and is given by

$$D = \frac{d\tau(\lambda)}{d\lambda} \tag{5.9}$$

The dispersion of a single-stage lossless all-pass filter is,

$$D = \frac{d}{d\lambda}\left[\frac{T_{rt}}{\frac{1-\sqrt{R}}{1+\sqrt{R}} + \frac{4\sqrt{R}}{1-R}\cos^2\left(\pi\frac{c}{\lambda}T_{rt}\right)}\right] \tag{5.10}$$

$$D = \frac{\pi}{c}(\nu T_{rt})^2\left(\frac{4\sqrt{R}}{1-R}\right)\frac{\sin(2\pi\nu T_{rt})}{\left[\frac{1-\sqrt{R}}{1+\sqrt{R}} + \frac{4\sqrt{R}}{1-R}\cos^2(\pi\nu T_{rt})\right]^2} \tag{5.11}$$

The dispersion *D* is inversely proportional to the square of FSR. As a result, increasing the FSR or the channel passband width comes at the expense of reduction in dispersion. Increasing the number of rings i.e. cascading many single-stage filters will increase dispersion linearly with the number of stages [42]. Multi-stage all-pass filters can be realized by cascading single stages [42-45].

A nine-stage dispersion compensating all-pass filter with FSR of 100 GHz is modeled using ring resonators to provide a dispersion of ~ +160 ps/nm over a passband width of about 45 GHz. Figure 5.2 shows a nine-stage all-pass filter design.

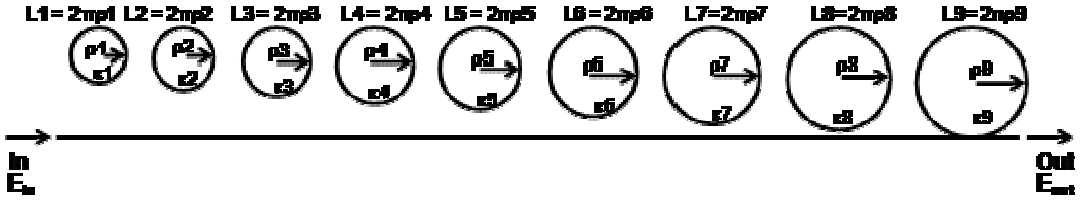

Fig.5.2. Schematic of cascaded nine-stage multi-channel dispersion compensating filter.

In a ring cascade structure, each ring is independently coupled to the waveguide. When 9 stages are cascaded, the resulting phase response is given by,

$$\varphi(\omega) = \sum_{i=1}^{9} \frac{\omega L_i}{c_{ph}} - 2\tan^{-1}\left[\frac{r_i \sin\left(\frac{\omega L_i}{c_{ph}}\right)}{1 + r_i \cos\left(\frac{\omega L_i}{c_{ph}}\right)}\right] \tag{5.12}$$

The group delay is the derivative of the phase with respect to the angular frequency. For a nine-stage lossless all-pass filter, the group delay is given by,

$$\tau = \sum_{i=1}^{9} \frac{T_i^{rt}}{\frac{1-\sqrt{R}_i}{1+\sqrt{R}_i} + \frac{4\sqrt{R}_i}{1-R_i}\cos^2\left(\pi\nu T_i^{rt}\right)} \tag{5.13}$$

The dispersion is the derivative of group delay with respect to wavelength and, the nine-stage filter dispersion is given by,

$$D = \sum_{i=1}^{9} \frac{\pi}{c}\left(\nu T_i^{rt}\right)^2 \left(\frac{4\sqrt{R_i}}{1-R_i}\right) \frac{\sin\left(2\pi\nu T_i^{rt}\right)}{\left[\frac{1-\sqrt{R_i}}{1+\sqrt{R_i}} + \frac{4\sqrt{R_i}}{1-R_i}\cos^2\left(\pi\nu T_i^{rt}\right)\right]^2} \tag{5.14}$$

The maximum group delay (peak) occurs at resonance frequency, which is determined by the length of the cavity. For a single-stage all-pass filter, in order to achieve an FSR of 100 GHz, the cavity length needs to be 2 mm (FSR = c_g/L). The length of each of the ring cavities is varied by a very small amount so that the maximum group delay of each ring cavity occurs at a slightly different resonance frequency (bottom part of Fig. 5.3 (a)). The nine single-stages are cascaded and the coupling coefficients κ_i and the ring radii ρ_i are chosen optimally for each ring so that the group delay response of cascaded nine rings is linear over a large portion of the channel passband width.

The optimized values of coupling coefficient and length for each of the 9 rings, to achieve a linear group delay response and a constant dispersion response over a passband width of about 45 GHz (~ FSR/2), are listed in Table 5.1.

Table 5.1. Optimized design parameters for a nine-stage all-pass filter with a 100 GHz FSR and 45 GHz passband width.

Ring#	Cavity Length (mm)	Coupling Coefficient
1	2.000000	0.82
2	2.000060	0.825
3	2.000140	0.83
4	2.000220	0.89
5	2.000300	0.91
6	2.000387	0.93
7	2.000475	0.95
8	2.000575	0.955
9	2.000670	0.957

Figure 5.3(a) shows the simulated group delay response of each of the nine rings (bottom part of Fig. 5.3(a)) and group delay response of cascaded nine-stage all-pass filter (top part of Fig. 5.3(a)). For a cascaded nine-stage all-pass filter with a100 GHz channel spacing, the variation in dispersion (ripple) is about ± 3 ps/nm over the passband width of 45 GHz.

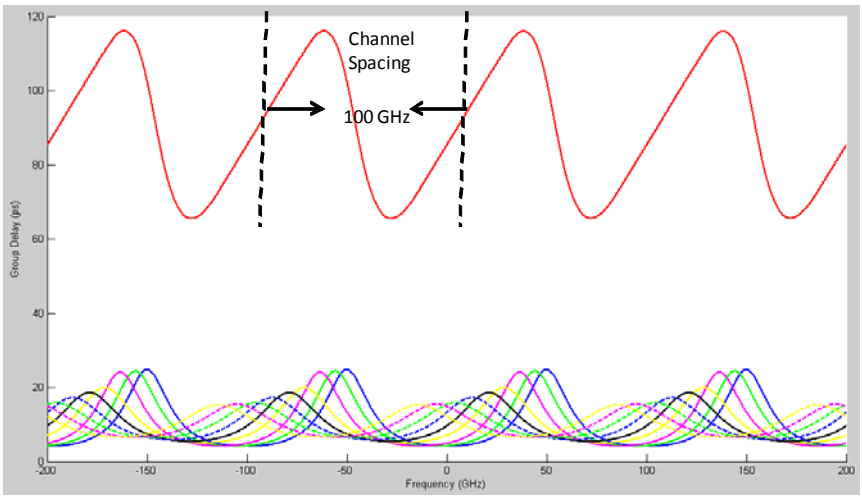

(a)

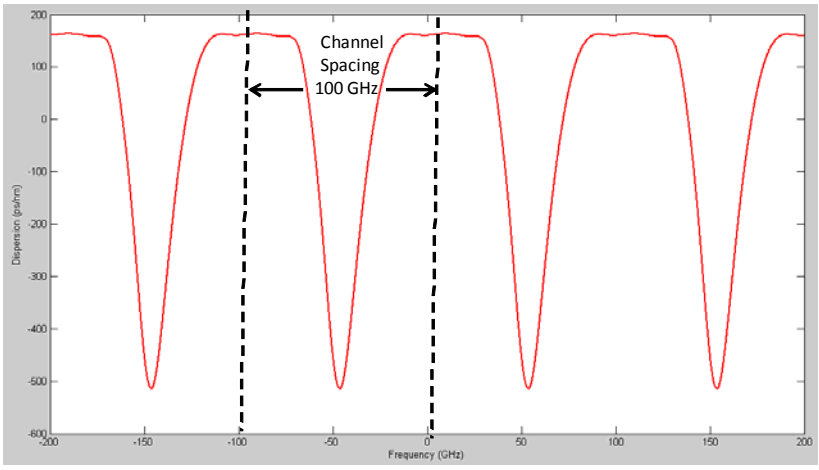

(b)

Fig. 5.3. Simulated (a) periodic group delay response of 9 individual single-stage all-pass filter (bottom part) and periodic group delay response of cascaded nine-stage all-pass filter (top part), (b) dispersion for multi-channel nine-stage all-pass filter.

To summarize, a nine-stage multi-channel dispersion compensating all-pass filter with FSR of 100 GHz and passband width of 45 GHz is designed using ring resonators. As seen in Fig. 5.3(a), the filter has a periodic group delay response and as a result, this

device can be used as periodic group delay device (PGDD) in our 2R regenerator. A constant dispersion of ~ +160 ps/nm is achieved over a passband width of about 45 GHz (~ FSR/2) and, the +160 ps/nm dispersion value is sufficient to compensate the dispersion of HNLF in our 2R regenerator. The next step in this research work is fabrication of 2R regenerator on a single chip using a planar waveguide technology.

CHAPTER 6

CONCLUSIONS

This dissertation has focused on experimental demonstration of simultaneous 2R regeneration of multiple WDM channels in a dispersion-managed configuration of Mamyshev's regenerator.

We have experimentally demonstrated single-channel 2R regeneration in a dispersion-managed configuration of Mamyshev's regenerator. In single-channel experiment, we used a 0.5-km-long piece of DCF as a nonlinear medium. To compensate its dispersion, we employed a combination of SSMF and NZDSF fibers. The regenerated signal was characterized after 15 circulations in the loop. We have observed an eye-opening improvement of 3 dB for signal with ±25% amplitude jitter and 2.5 dB for signal with poor extinction ratio. These results show that dispersion management does not degrade single-channel 2R performance.

We have experimentally demonstrated, for the first time, to our knowledge, the simultaneous 2R regeneration of 12 x 10 Gb/s WDM channels. For this task, we have designed a recirculating loop to work with just few hundred meters of fiber and, we believe, this is a novel application of recirculating loop to simulate a single-device consisting of multiple identical sections. In all our multi-channel experiments (2- , 8-, and 12-channel), 1.25 km of DCF was used as a nonlinear medium and PGDD was used as a dispersive medium. The regenerated signal was characterized after 5 circulations in

the loop for 12-channel case and 6 circulations for 2- and 8-channel cases. We have observed an eye-opening improvement greater than 2 dB for all 12 channels.

We have studied performance of our regenerator with respect to filter detuning and have observed that regenerator is robust to moderate change in filter detuning. In addition, we have measured the input-output transfer function of our regenerator. The regenerator has a nonlinear transfer function with a flat plateau as predicted by the 2R regenerator theory [2] and is capable of suppressing noise in "zeros" and the amplitude fluctuations in "ones" of return-to-zero (RZ) optical data streams. Furthermore, we have characterized the performance of our multi-channel regenerator with respect to the number of neighboring channels. We have varied the number of neighboring channels from 1 to 11, and have observed no degradation due to neighboring channels, and an eye-opening improvement better than 2 dB for all the cases. This shows that our regenerator scheme is scalable to large number of channels, which promises dramatic reduction in size, cost, and power consumption of optical communication systems.

APPENDIX A

TERAXION CLEARSPECTRUM™ -TDC

PGDD: Teraxion's ClearSpectrum™-TDC

As mentioned in chapter 4, the periodic group delay device (PGDD), a key component of our 2R regenerator, used in our experiments is Teraxion's custom made Tunable Chromatic Dispersion Compensator "ClearSpectrum- TDC27-1527.216-200 (-0250/+0250) A01. This tunable PGDD device operation is based on multi-CFBGs (chirped fiber Bragg gratings) used in reflection and requires a 4 port optical circulator to collect the dispersion compensated signal and separate it from the input signal. Teraxion's tunable dispersion compensator (TDC) is a 27-channel device with 200 GHz channel spacing, covering ITU frequencies from 191.1 THz (1568.8 nm) to 196.3 THz (1527.2 nm).

The operation of TDC is based on the thermal control of the CFBGs. The ClearSpectrum-TDC package contains two Thermoelectric Coolers (TECs) and one heating element. Three RTDs are used as temperature sensors for two TECs and one heater, respectively. Figure 1 shows the diagram of arrangement of TECs, heater and RTDs inside the ClearSpectrum-TDC module.

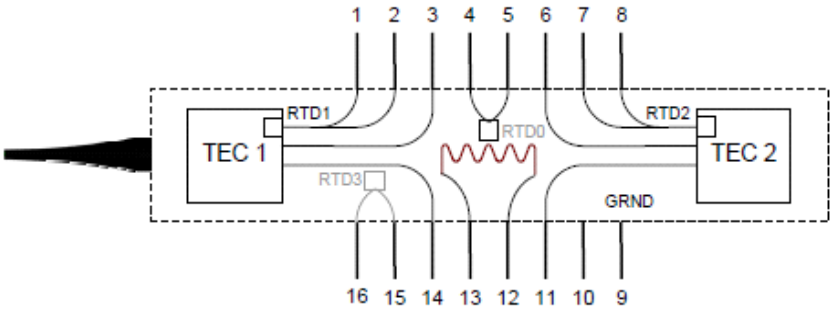

Fig. 1. Schematic showing the arrangement of TECs, Heater and RTDs inside the module [Figure from ClearSpectrum-TDC User's Guide].

Three temperature controllers are used to control the temperatures of two TECs and a heating element. The temperature controllers are manually adjusted to achieve the desired dispersion level. The three temperature controllers, required to operate the TDC, used in our experiments are Wavelength Electronics “LFI-3751 with Autotune PID Thermoelectric Temperature Controllers". Two of the three temperature controllers (LFI-3751) used in our experiments have auto-tune optimization option and for the third controller, we need to set the PID (P: Proportional gain, I: Integrator time constant, and D: Differentiator time constant) values manually. Table 1 lists the PID settings used on each of these controllers.

LFI-3751 configuration parameters used with Teraxion’s ClearSpectrum-TDC

Parameters	TEC1	TEC2	Heater
P	21	21	16
I	0.6	0.6	2.0
D	0	0	0
A	1, 1	1, 1	1, 1
B	0°C, 1.000 KΩ	0°C, 1.000 KΩ	0°C, 1.000 KΩ
C	100°C, 1.385 KΩ	100°C, 1.385 KΩ	100°C, 1.385 KΩ
Current limits	-1.4 A and +1.4 A	-1.4 A and +1.4 A	-0.4 A and +0.0 A

To ensure that the TDC functions properly, the TECs should be operated below their maximum current and temperature limits. The maximum current and voltage these TECs can handle is 1.4 A and ± 4.0 V, respectively. Also, TEC’s steady-state temperature should never exceed 130°C and the temperature on the heater should always be less than 100°C. To indicate that the sensor is an RTD, the parameter A is set to (1.000, 1.000). Also, the LFI-3751 requires us to specify two data points B = (T2,

R2) and C = (T3, R3) to calculate the RTD resistance from the setpoint temperature, using the specified values of constants and the Callendar - Van Dusen equation ($R_{RTD} = R_0 [1+AT+BT^2+CT^3]$). A table specifying the values of constants R_0, A, B, and C, and also, a table showing the correlation between RTD resistance and temperature are given in the ClearSpectrum-TDC User's Guide.

To obtain the desired dispersion level, we set the temperatures in the TEC1 and TEC2 controllers to the temperature values specified in the lookup table provided by Teraxion. The heater temperature is always maintained at a fixed value of 67°C. The desired dispersion level is achieved as soon as the temperatures are stabilized at the set values. However, the temperature controllers used in our experiments, do not settle accurately at the specified setpoint temperature. As the dispersion of TDC is very sensitive to temperature, it is necessary that the controllers settle exactly at the specified setpoint temperatures. Therefore, it is necessary to determine the offset, the difference between the setpoint and the actual or achieved temperature, and then accordingly adjust setpoint temperature. As an example, assume that the heater has a setpoint temperature of 67°C but the settled temperature is 66.90 °C. Then, we need to enter an offset compensation factor for this difference of 0.10 °C into its setpoint temperature. As a result, the operational setpoint temperature would be 67.10 °C in order to achieve the final, settled 67.0 °C actual temperature. This temperature check should be performed for each TEC and the heater.

In our multi-channel experiments, the dispersion at the PGDD was set to +170 ps/nm to compensate the dispersion of DCF such that the residual dispersion per loop is

about +20 ps/nm. To obtain the dispersion of +170 ps/nm, we need to set the the temperatures at TEC1, TEC2, and heater at: TEC1= 78 °C, TEC2 = 53.8 °C and heater = 67.0 °C. Using this device in our experimental set up, we observed our first multi-channel regeneration results in February 2008. From February 2008 to July 2008, we did not see any signal regeneration and this was because the channel center wavelengths (CCWs) of ClearSpectrum-TDC had slowly drifted from their original values. Before employing the ClearSpectrum-TDC in our experiments, in October 2007 we had observed its spectrum at an Optical Spectrum Analyzer (OSA) and had recorded the CCWs. After operating the device continuously for about 7 months with +170 ps/nm dispersion, in June 2008 we again observed its spectrum at OSA and noticed that the CCWs had drifted by about ~ 0.3 nm toward shorter wavelengths from their original centers. Table 2 lists the original CCWs and the new drifted CCWs, measured at OSA using a resolution bandwidth of 0.2 nm.

Drift in PGDD channel center wavelengths measured for +170 ps/nm dispersion.

Channel #	Original channel center wavelength (nm) Recorded in October, 2007	New channel center wavelength (nm) Recorded in June, 2008	Channel center wavelength drift (nm)
1	1542.83	1542.54	0.29
2	1544.41	1544.11	0.30
3	1545.99	1545.68	0.31
4	1547.58	1547.25	0.32
5	1549.18	1548.84	0.34
6	1550.80	1550.44	0.36
7	1552.40	1552.04	0.36
8	1554.03	1553.67	0.36
9	1555.65	1555.30	0.35
10	1557.27	1556.94	0.33
11	1558.89	1558.58	0.31
12	1560.51	1560.20	0.30

We speculated many reasons for this drift in the TDC's CCWs like, may be the device is damaged or may be the TECs or the RTDs are damaged or maybe it's just because of the constant use of device for about 7 months. When we contacted the personnel at Teraxion, they suggested that this could potentially be caused by a defective heater. One way to test if the heater is operating correctly is to measure the resistance of the heater (across pin 12 and pin 13) using a multimeter. The resistance of the heater should be approximately 30 Ω. Another method to test if the heater is functioning properly is to measure the heater RTD resistance (pins 4 and 5). The nominal resistance of the RTD is 1000 Ω at 0 °C and its resistance variation is 3.85 Ω per degree Celsius. Therefore, if the heater is working correctly then we should read approximately 1097 Ω at room temperature (about 25 °C). Also, we measured the variation of TEC1 RTD resistance (pins 1 and 2) and TEC2 RTD resistance (pins 7 and 8) with respect to temperature. The variation of TEC1, TEC2, and heater RTD resistance with temperature agrees with the RTD resistance vs. temperature table given in the ClearSpectrum-TDC User's Guide. After performing these tests, we found that the TECs and the heater are working properly. There could be a possibility that the gratings have lost contact with the thermal platform (TECs, heater, and RTDs). As a result, though the TECs, heater, and RTDs work well, if the grating is detached from the thermal platform then the grating temperature might be different than the temperature measured by RTDs or temperature displayed by temperature controllers.

We still do not know the actual reason that caused the shift in the TDC CCWs by about 0.3 nm towards the blue wavelengths. To use this device in our multi-channel

experiments, we had to adjust our channel plan accordingly by tuning the DFBs to the TDC's new channel centers. As we observed signal regeneration by tuning our DFBs to the TDC's new CCWs, we assume that the shift in channel center wavelengths did not affect the channel dispersion. Therefore, when we use this device in our experiments it is necessary to observe its spectrum every few months to know if there is any more drifting in TDC's CCWs.

APPENDIX B

12-CHANNEL 2R REGENERATION EXPERIMENT DEVICE SETTINGS

Transmitter:

1) Bit Error Rate Tester (BERT): Pattern Generator and Error Detector

Agilent 70843B 0.1 – 12 Gbit/s,

Error Performance Analyzer

i) Pattern: PRBS 2^{31}-1

ii) Gating: Gating repeat mode: Manual

Burst gating: ON

iii) Data Output: Termination: 0 V dc

Amplitude: 600 mV

$\overline{\text{Amplitude}}$: 600 mV

High-level: 0.00 V

$\overline{\text{High-level}}$: 0.00 V

External attenuation: 0.0 dB

iv) Clock Output: Termination: 0 V dc

Amplitude: 850 mV

$\overline{\text{Amplitude}}$: 850 mV

High-level: -900 mV

$\overline{\text{High-level}}$: -900 mV

External attenuation: 0.0 dB

v) Trigger and setup: Pattern generator trigger mode: Clock/8

Error detector trigger mode: Clock/8

Error detector output: RZ

An external 6 dB attenuator is used at the data output port of pattern generator.

2) Display: Hewlett Packard 70004A

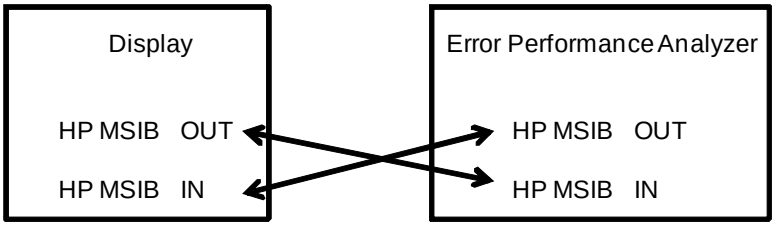

Figure. 1. Schematic showing the connections between the error performance analyzer and display units.

3) DFB frames: Photonetics OSICS

Note: All DFBs have PC connectors

4) Tunable Laser Source: ANDO AQ4321A

   i) Wavelength range: 1480 to 1580 nm

   ii) Power range: - 20 dBm to + 8 dBm

5) Modulators:

   a) JDS Uniphase, Dual stage 10 Gb/s NRZ data modulator with RZ pulse generator stage.

      i) Insertion loss: 4.9 dB

      ii) RZ bias : 1.1 V (bias value used in experiments)

      iii) NRZ bias: 6.4 V (bias value used in experiments)

   Note: Bias voltages tend to drift, as a result need to adjust these voltages slightly everyday to ensure we have clean 50% RZ pulse.

   b) Lucent Technologies, 40Gb/s Lithium Niobate Electro-optic Modulator

      i) Insertion loss: 6 dB

Note: In multi-channel 2R regeneration experiments, Lucent modulator is employed as a polarizer and as a result, we do not apply bias voltages to the modulator. The modulator is used after the 50/50 coupler (Fig. 4.17, 50/50 coupler combines channels modulated with different data pattern by two JDS modulators onto a single fiber) to ensure all channels are co-polarized.

6) Signal generator: Agilent Technologies E8257D 250 kHz – 20 GHz

PSG Analog Signal Generator

   i) Frequency: 9.956540 GHz

   ii) Amplitude: 8 dBm

7) AWGs: AC Photonics Inc (P/N: DWDM216MC192111)

   i) Insertion loss: < 3dB

   ii) Channel spacing: 200 GHz

Receiver:

1) Optical Band Pass Filter: JDS Uniphase, TB9226 Optical Grating Filter

   i) Tuning range: 1525 nm to 1625 nm

   ii) -3 dB bandwidth: 0.22 nm

   iii) Insertion loss: ≤ 4 dB

2) PIN photodetector: Agilent 11982A Lightwave Converter

   i) Wavelength range: 1200 nm to 1600 nm

   ii) Bandwidth: dc to 15 GHz (optical)

dc to 11 GHz (electrical)

3) Clock recovery: NEL MOS43BM 10 Gb/s Clock and Data Recovery Module

4) Digital Communication Analyzer (DCA): Hewlett Packard 83480A

OPT 100 Enhanced Trigger

Periodic Group Delay Device (PGDD):

1) Teraxion Tunable Dispersion Compensator: ClearSpectrumTM – TDC
    i) Model Number: TDC27-1527.216-200(-0250/+0250)A01
    ii) Dispersion tuning range: -250 ps/nm to +250 ps/nm
    iii) Number of channels: 27 (channel wavelength: 1527.216 to 1568.773 nm)
    iv) Channel spacing: 200 GHz (~ 0.16 nm)
    v) Insertion loss: 5.1 dB (Includes loss of 4-port optical circulator)
2) Temperature Controllers: Wavelength Electronics

LFI-3751 with Autotune PID

Thermoelectric Temperature Controllers

Erbium Doped Fiber Amplifiers (EDFAs):

1) IPG Photonics
    i) Optimized wavelength range: 1535 to 1570 nm
    ii) Typical input power (Pin): 10 dBm
    iii) Output power (Pout): 37 dBm
    iv) Gain: 27 dB
    v) Noise Figure (NF): 6 dB
2) INO Erbium Doped Fiber Amplifer
    i) Gain: 30 dB
3) Optocom Innovation Bauc BB Fiber Amplifier, Model 30 dBm, 1.5 μm

Digital Delay / Pulse Generators: Stanford Research Systems (SRS)

Model DG535

1) SRS1
   a) Trigger:
      i) TRIG: Internal
      ii) Rate: 12140 Hz (to observe 7 circulations)
   b) Delay:
      i) A: T + 0.000020
      ii) B: A + 0.000000 (currently in CW mode, need to increase to open the loop)
      iii) C: A + 0.000029 (circulation # 5)
      iv) D: C + 0.000003
   c) Output: T_0, A, B, AB, C, D, CD
      i) A: Load: High Z
         TTL
         Inverted Normal
      ii) B: Load: High Z
         TTL
         Inverted Normal
      iii) C: Load: High Z
         TTL
         Inverted Normal
      iv) D: Load: High Z

TTL

Inverted Normal

v) AB and – AB: Loads: High Z

AB: TTL

vi) CD and – CD: Loads: High Z

CD: TTL

2) SRS2

a) Trigger:

i) TRIG: External

ii) Threshold: + 1.00 V

iii) Slope (+/–): –

iv) Trigger term: High Z

b) Delay:

i) A: T + 0.000003

ii) B: A + 0.000010

iii) C: A + 0.000000

iv) D: C + 0.000003

c) Output: T_0, A, B, AB, C, D, CD

i) T_0: Load: High Z

TTL

Inverted Normal

ii) A: Load: High Z

TTL

Inverted Normal

iii) B: Load: High Z

TTL

Inverted Normal

iv) C: Load: High Z

TTL

Inverted Normal

v) D: Load: High Z

TTL

Inverted Normal

vi) AB and – AB: Loads: High Z

AB: TTL

vii) CD and – CD: Loads: High Z

CD: TTL

REFERENCES

[1] M. Vasilyev and T. I. Lakoba, "All-optical multichannel 2R regeneration in a fiber-based device," Opt. Lett. **20**, 1458 (2005).

[2] P.V. Mamyshev, "All-optical data regeneration based on self phase modulation effect," *24th European Conference on Optical Communication* (Institute of Electrical and Electronics Engineers, 1998), Vol.1, pp. 475−476.

[3] R. Ramaswami and K N. Sivaranjan, *Optical Networks*, 2nd ed., Academic Press, San Francisco, 2002.

[4] M. J. Yadlowsky, E. M. Deliso, and V. L. Da Silva, "Optical Fibers and Amplifiers for WDM Systems," in *Proceedings of THE IEEE*, Vol.85, pp.1765-1779, November 1997.

[5] G. P. Agrawal, *Nonlinear Fiber Optics*, 3rd ed., Academic Press, San Diego, 2001.

[6] B. E. A. Saleh and M. C. Teich, *Fundamentals of Photonics*, 2nd ed., Wiley & Sons, 2007.

[7] G. P. Agrawal, *Fiber Optic Communication Systems*, 3rd ed., Wiley & Sons, New York, 2002.

[8] F. Forghieri, R. W. Tkach, and A. R. Chraplyvy, "Fiber Nonlinearities and Their Impact on Transmission Systems," in *Optical Fiber Telecommunications IIIA*, I. P. Kaminow and T. L. Koch, Academic Press, San Diego, 1997, pp. 196−254.

[9] A. R. Chraplyvy, "Limitations on Lightwave Communications Imposed by Optical-Fiber Nonlinearities," in *J. Lightwave Technol.*, Vol.85, pp.1548-1557, October 1990.

[10] G. Keiser, *Optical Fiber Communications*, 4th ed., Tata McGraw-Hill, 2008

[11] E. A. Golovchenko, N. S. Bergano, and C. R. Davidson, “Four-Wave Mixing in Multispan Dispersion-Managed Transmission Links,” in *IEEE Photon. Technol. Lett.*, Vol.10, pp.1481-1483, October 1998.

[12] S. Watanabe, and F. Futami, “Optical Signal Processing with Nonlinear Fibers,” *Optical Fiber Communications* conference 2003, paper TuQ1.

[13] O. Leclerc, B. Lavigne, D. Chiaroni, and E. Desurvire, “All-optical regeneration: principles and WDM implementation,” in *Optical Fiber Telecommunications IVA*, I. P. Kaminow and T. Li, Eds., Academic Press, San Diego, 2002, pp. 732−783.

[14] B. E. Olsson, P. Ohlen, L. Rau, and D. J. Blumenthal, “A simple and robust 40-Gb/s wavelength converter using fiber cross-phase modulation and optical filtering,” *IEEE Photon. Technol. Lett.*, vol. 12, pp. 846–848, July 2000.

[15] E. Ciaramella and S. Trillo, “All-optical signal reshaping via four-wave mixing in optical fibers,” *IEEE Photon. Technol. Lett.*, vol. 12, pp.849–851, July 2000.

[16] P. Brindel, B. Dany, O. Leclerc and E. Desurvire, “Black box optical regenerator for RZ transmission systems,” in *IEEE. Electron. Lett*. 35, pp.480-577, June 2007.

[17] M. Matsumoto, and O. Leclerc, “Analysis of 2R optical regenerator utilizing self-phase modulation in highly nonlinear fibre,” in *IEEE. Electron. Lett*. 38, pp.576-577, June 2004.

[18] M. Matsumoto, “Performance analysis and comparison of optical 3R regenerators utilizing self-phase modulation in fibers,” in *J. Lightwave Technol.*, Vol.22, pp.1472-1482, June 2004.

[19] D. I. Kovsh, L. Liu, B. Bakhshi, A. N. Pilipetskii, E. A. Golovchenko, and N. S. Bergano, “Reducing interchannel crosstalk in long-haul DWDM systems,” in *J. Lightwave Technol.*, Vol.8, pp.597-602, June 2002.

[20] T. Ohara, H. Takara, A. Hirano, K. Mori, and S. Kawanishi, "40-Gb/s × 4-channel all-optical multichannel limiter utilizing spectrally filtered optical solitons," in *IEEE Photon. Technol. Lett*. 15, 763-765 (2003).

[21] K. Cvecek, K. Sponsel, C. Stephan, G. Onishchukov, R. Ludwig, C. Schubert, B. Schmauss, and G. Leuchs, "Phase-preserving amplitude regeneration for a WDM RZ-DPSK signal using a nonlinear amplifying loop mirror," in *Opt. Express.* 16, 1923-1928 (2008).

[22] L. Provost, F. Parmigiani, C. Finot, K. Mukasa, P. Petropoulos, and D. J. Richardson, "Analysis of a two-channel 2R all-optical regenerator based on a counter-propagating configuration," in *Opt. Express.* 16, 2264-2275 (2008).

[23] L. Provost et al, "Investigation of four-wavelength regenerator using polarization-and-Direction-Multiplexing," in *IEEE Photon. Technol. Lett*. 20, 1676-1678 (2008).

[24] C. Kouloumentas *et al*, "Four-channel all-fiber dispersion-managed 2R regenerator," IEEE Photon. Technol. Lett. 20, 1169 (2008).

[25] J. Zyskind, R. Barry, G. Pendock, M. Cahill, and J. Ranka, "High-capacity, ultra-long-haul networks," in *Optical Fiber Telecommunications IVB*, I. P. Kaminow and T. Li, Eds., Academic Press, San Diego, 2002, pp.198−231.

[26] M. Guy, F. Trepanier, A. Doyle, Y. Painchaud, and R.L. Lachance, "Novel applications of fiber Bragg grating components for next-generation WDM systems," in *Annals of Telecommunications*, Springer, Vol. 58, No. 9-10, September 2003, pp. 1275-1306.

[27] S. Lelievre, E. Pelletier, A.W. Farr, Y. Painchaud, R.L.Lachance, and M. Brown, "Grating-based solutions for chromatic dispersion management in DWDM systems," in *National Fiber Optic Engineers Conference*, September 2002.

[28] R. L. Lachance, Y. Painchaud, and A. Doyle, "Fiber Bragg Gratings and Chromatic Dispersion," in *International Conference on Applications of Photonics*, June 2002.

[29] Y. Painchaud, M. Lapointe, and M. Guy, "Slope-matched tunable dispersion compensation over the full C-band based on fiber Bragg gratings," in *24th European Conference on Optical Communication*, 2004, paper We3.3.4.

[30] Y. Painchaud, C. Paquet, and M. Guy, "Optical tunable dispersion compensators based on thermally tuned fiber Bragg gratings," in *Optics and Photonics News*, Vol. 18, pp. 48-53, September 2007.

[31] Y. Painchaud, M. Lapointe, F. Trepanier, R. L. Lachance, C. Paquent, and M. Guy, "Recent progress on FBG-based tunable dispersion compensators for 40 Gb/s applications," in *Proceedings of OFC*, 2007, paper OThP3.

[32] G. Bellotti and S. Bigo, "Cross-phase modulation suppressor for multispan dispersion-managed WDM transmission," IEEE Photon. Technol. Lett. 12, 726–728 (2000).

[33] G. Bellotti, S. Bigo, P. Y. Cortes, S. Gauchard, and S. LaRochelle, "10x10 Gb/s Cross-phase modulation suppressor for multispan transmissions using WDM narrow-band fiber Bragg gratings," IEEE Photon. Technol. Lett. 12, 1403–1405 (2000).

[34] X. Wei, X. Liu, C. Xie, and L. F. Mollenauer, "Reduction of collision-induced timing jitter in dense wavelengthdivision multiplexing by the use of periodic-group-delay dispersion compensators," Opt. Lett. 28, 983–985 (2003).

[35] L. F. Mollenauer, A. Grant, X. Liu, X.Wei, C. Xie, and I. Kang, "Experimental test of dense wavelength-division multiplexing using novel, periofic-group-delay-complemented dispersion compensation and dispersion-managed solitons," Opt. Lett. **28**, 2043–2045 (2003).

[36] T. I. Lakoba, and M. Vasilyev, "A new robust regime for a dispersion-managed multichannel 2R regenerator," Opt. Express 15, pp.10061-10074, July 2007.

[37] M. Vasilyev, M. Mehendale, and S. Tsuda, "Optimum pre-emphasis in ultra-long-haul networks," in *Journal of Optical Networking*, Vol.5, pp.159-174, March 2006.

[38] C. Madsen, G. Lenz, A. Bruce, M. Capuzzo, L. Gomez, and R. Scotti, "Integrated all-pass filters for tunable dispersion and dispersion slope compensation," IEEE Photon. Technol. Lett., vol. 11, pp. 1623–1625, Dec. 1999.

[39] C. R. Doerr, L. W. Stulz, S. Chandrasekhar, L. L. Buhl, and R. Pafchek, "Multichannel integrated tunable dispersion compensator employing a thermooptic lens," in Tech. Dig. OFC 2002, paper PD-FA6.

[40] M.Vasilyev, T. I. Lakoba, and P. G. Patki, "Multi-wavelength all-optical regeneration," *Optical Fiber Communications* conference 2008, paper OWK3.

[41] C. R. Doerr, and K. Okamoto, "Planar lightwave circuits in fiber-optic communications," in *Optical Fiber Telecommunications VA*, I. P. Kaminow, T. Li, and A. E. Willner, Academic Press, San Diego, 2008, pp.269−338.

[42] C. Madsen, G. Lenz, A. Bruce, M. A. Capuzzo, L. T. Gomez, T. N. Nielsen, and I. Brener, "Multi-stage dispersion compensator using ring resonators," Opt. Express 24, pp.1555-1557, November 1999.

[43] G. Lenz, and C. K. Madsen, "General optical all-pass filter structures for dispersion control in WDM systems," in *J. Lightwave Technol.*, Vol.17, pp.1248-1254, July 1999.

[44] C. K. Madsen, E. J. Laskowski, J. Bailey, M. A. Capuzzo, S. Chandrasekhar, L. T. Gomez, A. Griffin, P. Oswald, and L. W. Stulz, "The application of integrated ring

resonators to dynamic dispersion compensation" in *Proc. IEEE/LEOS All-Optical Networking*, Jul. 15–17, 2002, p. 2–29.

[45] C. K. Madsen, G. Lenz, A. J. Bruce, M. A. Capuzzo, L. T. Gomez, T. N. Nielsen, L. E. Adams, and I. Brenner, "An all-pass filter dispersion compensator using planar waveguide ring resonators," in *Proceedings of OFC*,1999, San Diego, CA, Feb. 20-26, 1999, Paper FE6.

BIOGRAPHICAL INFORMATION

Pallavi received her Bachelor of Engineering degree in Electronics and Communications from Basaveshwar Engineering College, Bagalkot, India and her Master of Science degree in Electrical Engineering from the University of Texas, Arlington (UTA). At UTA, she was president of Optical Society of America (OSA) student chapter for 2008 - 2009.

During her internship (Summer 2009) at IBM T. J. Watson Research in Yorktown Heights, NY, she studied the performance of multi-channel CWDM transceivers. During the summer of 2010, she worked at Corning Inc, NY, on 100-Gb/s coherent systems using polarization-division multiplexed QPSK and 16-QAM modulations. Her research interests include all-optical signal processing, nonlinear optics, and fiber-optic communications.